The effect of Cenozoic basin inversion on coal-bed methane in Liupanshui Coalfield, Southern China

Biying Chen[1,2], Finlay M. Stuart[1*], Sheng Xu[1,2*], Domokos Györe[1] and Congqiang Liu[2]

[1] Scottish Universities Environmental Research Centre (SUERC), East Kilbride, G75 0QF, United Kingdom

[2] Institute of Surface-Earth System Science, School of Earth System Science, Tianjin University, Tianjin 300072, China

[*]Author for correspondence: fin.stuart@glasgow.ac.uk (Finlay Stuart), sheng.xu@tju.edu.cn (Sheng Xu)

Abstract

Coalbed methane (CBM) is an important energy source globally, thus understanding its origin and evolution is essential to the assessment of reserves and developing exploration strategies. This study aims to identify the origin of CBM in Liupanshui Coalfield (LPC) in southern China and evaluate the influence of basin exhumation on gas storage in different rank coals. Ten CBM samples were collected from four blocks that have different thermal histories and coal rank ranges. Based on the $C_1/(C_2+C_3)$ ratio (16-971), $\delta^{13}C_{CH4}$ (-42.9 to -34.9‰) and δD_{CH4} (-206 to -140‰), the methane is mainly thermogenic in origin. Systematic compositional differences between the four blocks are consistent with coal maturity. Noble gases in LPC CBM are a mixture of air-derived gas dissolved in local groundwaters and radiogenic gases that were generated in the coals and diffused in from deeper crust. The radiogenic $^{4}He/^{40}Ar^{*}$ and $^{21}Ne^{*}/^{40}Ar^{*}$ are lowest in CBM from Qingshan block, strong evidence of diffusive loss of light noble gases. $^{20}Ne/^{36}Ar$ (0.23-0.70) in all gases are higher than local air-saturated water (0.16) and are most easily explained by re-dissolution of noble gases that exsolved from groundwater during basin inversion. $^{84}Kr/^{36}Ar$ and $^{132}Xe/^{36}Ar$ ratios are higher than predicted from this process and likely reflect desorption of Xe and Kr that has been trapped on the coal matrix at the time of coal desorption. The noble gases are consistent with gas exsolution and loss from the reservoir during Mesozoic-Cenozoic basin inversion. Modelling the loss of both free and adsorbed gas during basin inversion we find that the Qingshan block has lost the highest proportion of free gas (77%), yet the total gas loss (free and adsorbed) is the lowest (25%) due to the strong adsorption capacity of the mature coals. The volume of groundwater that has interacted with the gas phase during the basin inversion is estimated according to the re-dissolution process model to evaluate the role of groundwater in gas preservation and gas extraction. Combining gas production data for the four blocks, high gas content and efficient gas extraction in LPC are expected for the high maturity coals that have seen low groundwater during basin inversion but more at shallow depth.

Keywords

Coalbed methane, noble gas isotopes, gas loss, Liupanshui coalfield, SW China

1. Introduction

Coalbed methane (CBM) is a natural gas resource generated and stored in coal beds (Levine, 1993; McGlade et al., 2013; Rice et al., 1989). The commercial extraction of CBM once contributed 10% of natural gas production in the USA (EIA, 2010) and remains a valuable global energy supply. Geochemical and stable isotope studies of CBM have revealed much about gas generation processes and subsequent evolution, e.g., the addition of external hydrocarbons and gas escape, which are critical to the estimation of resource potential, and assessing potential environmental impacts on its exploitation (e.g., Liu et al., 2019; Moore, 2012; Vinson et al., 2017; Zazzeri et al., 2016). While the trace noble gases have been used extensively to trace the origin and interaction history of fluids in conventional petroleum and natural gas systems (e.g., Ballentine et al., 1991; Battani et al., 2000; Scott et al. 2021), their application on CBM is limited. Previous studies have shown that noble gases can track the role of groundwater in CBM production and constraint the timescale of hydrogeological processes that have affected hydrocarbon preservation (Zhou and Ballentine, 2006; Zhou et al., 2005). They have been used to identify the exogenous gas in the reservoir and improve the understanding of the origin of methane (Moore et al., 2018). The presence of mantle-derived volatiles in CBM deposits provides constraints on local intrusions and their role in the thermal maturation (Györe et al., 2018).

The low He content of ultra-mature coals (R_o= 2.4-4.5%) in southeast Qinshui Basin has revealed a discernible loss of free gas prior to gas extraction, likely caused by intensive basin inversion in Miocene (Chen et al., 2019). While this event had a negligible influence on methane storage, the effect on lower maturity coals remains untested. The Liupanshui Coalfield (LPC) in Guizhou Province, southern China, is a promising CBM exploitation region. The basin was separated into several blocks during the main stage of Yanshanian Orogeny in the Late Jurassic-Early Cretaceous. Since then these blocks have experienced different burial and exhumation histories such that the coals in each block have markedly different maturity (Dou, 2012). CBM extraction occurs in many blocks. Consequently, LPC is an ideal site for studying generation, preservation and transport of natural gas during and after basin inversion in different mature coals.

Here we report the results of the study of the geochemistry and isotope composition of CBM from the four main blocks in LPC. We use the stable isotope and the major gas composition of gas from the coalfield to trace the origin of methane. The noble gases provide an understanding

of the gas transport and retention during basin inversion and allow the evaluation of the extent of gas loss in each block.

2. Liupanshui Coalfield

2.1 Geological setting

The Liupanshui Coalfield is located on the passive southern margin of the upper Yangtze platform, covering an area of 1.5×10^4 km^2 in western Guizhou Province (Figure 1) (Gui, 1999; Xu, 2012). The major mineable coal in the region is located in the Permian Lopingian Longtan and Changxing (also called Wangjiazhai in local blocks) formations (Figure 2). The Longtan formation unconformably overlies Guadalupian Emeishan basalts. Following several cycles of marine transgression and regression during the Lopingian, several thick coal beds were deposited in a deltaic-lagoon sedimentary environment. During the Early-Mid Triassic 3,500-5,000 m of marine sediments were deposited (Dou, 2012). This was followed by a regional regression and deposition of terrestrial sediments at the end Mid Triassic. Upper Triassic clastic rock and lower-middle Jurassic mudstones and sandstones are present in the Shuicheng and Langdai area (northern LPC). Paleogene and Neogene lacustrine deposits are observed around Panxian and Puan (Figure 1) (Zhang, 2017). There are sparse Quaternary deposits distributed in the coalfield.

Permian Guadalupian limestones in Maokou and Qixia formations and lower Triassic limestones in Yongningzhen Formation and dolomites in Guanling Formation have well-developed cave systems and act as the main aquifer layers within the LPC (Bao, 2019; Zhang, 2017). The coal-bearing strata are sealed by the overlying Feixianguan mudstones and underlain Emeishan basalts (Figure 2), which limits water recharge and benefits gas preservation in coal seams (Xu, 2012; Zhang, 2017).

2.2 Burial and thermal evolution history

The burial history and thermal evolution of the LPC coal seams are constrained by stratigraphy, coal mineralogy and geothermal gradients, exploration information and coal R_o values (Dou, 2012; Tang et al., 2016; Ju et al., 2021). The thermal history models presented by Dou (2012) indicate that prior to the Late Jurassic, the LPC experienced two stages of burial (Figure 3A). The first occurred in the Upper and Middle Triassic resulting in the first

stage of coal maturation. It was followed by basin inversion in the Late Triassic due to the Anyuan Movement. Deposition that started in the Early Jurassic exceeded the initial burial depth reached in the Middle Triassic, inducing further coal maturation. This is inconsistent with the work of Tang et al. (2016), which considered that Late Triassic basin inversion was not significant and maximum burial depth of coal seams was reached in the Early Cretaceous. Despite this, the maximum burial depth that coals in Panxian (a research site common to both studies) reached in the two models are similar. The time and amount of erosion after the maximum burial are similar in both models.

Magmatic activity during the main stage of Yanshanian orogenic event (Late Jurassic to Early Triassic) is argued to have enhanced the coalification process in some parts of the LPC as the maximum burial depth of coals with a normal thermal gradient of 25-30°C/km could not explain the measured R_o of coals (Dou, 2012). The maximum homogenisation temperatures of aqueous fluid inclusions in vein quartz from the roof and floor of coal seams in Panxian (135-150°C) also could not have been reached by maximum burial (3,500 m) with a normal thermal gradient, implying the occurrence of hydrothermal fluid flow generated by Yanshanian magmatism in the deep crust (Tang et al., 2016). The Yanshanian-aged dolerite (115 Ma) in the Pannan anticline, southwest of Guizhou (Chen, 1995; Dou, 2012), is strong evidence that magmatism-driven enhanced geothermal gradient may have existed at the time.

The Yanshanian and Himalayan orogenesis resulted in folding and faults, destroying the prototype of the basin (Dou, 2012; Gui, 1999; Tang et al., 2016). The coal seams in the anticline system were mostly eroded during Himalayan uplift. The coal seams in syncline and synclinoria blocks in LPC have experienced different burial histories, which has resulted in a wide range of maximum R_o values ($R_{o,max}$) of coals, from 0.7 to 3.4% (Dou, 2012; Tang et al., 2016).

The Qingshan syncline block (QI) occupies ~1,010 km^2 at the southern end of the coalfield (Figure 1E) (Lei et al., 2012; Wen et al., 2008). According to the modelling results in Dou (2012), the burial in the Early and Middle Triassic to 5,000 m led to the reservoir temperature reaching ~140°C (R_o=0.8-1.0%). Further burial in the Early-Middle Jurassic increased reservoir temperature to over 160°C (R_o=1.2-1.4%). Since the Late Jurassic, the basin experienced uplift and erosion. In the Early Cretaceous, a thermal pulse heated the coal-bearing strata to about 240°C, maturing the coal seams to semi-anthracite grade (R_o >2%). Basin inversion resulted in the erosion of 3,200 m during the Cenozoic bringing the coal seams to

depths of less than 1,000 m. The $R_{o,max}$ of the coals is the highest in the region, 1.7-3.0% (Lei et al., 2012; Wen et al., 2008).

The Dahebian syncline block (DA) occupies ~130 km^2 (Figure 1B) (Bao, 2019). There are approximately 40 coal seams with a minable thickness of ~20 m. There are 16-33 coal layers with a mineable thickness of up to 21.3 m. The model in Dou (2012) reveals that tectonic history before the Late Jurassic in this block is similar to Qingshan block except for a lower maximum burial depth and less inversion. The Late Jurassic thermal pulse coincided with the main phase of basin inversion (~2,300 m). Since then 500-600 m of basin inversion has occurred, and the coal seams have not experienced further coalification. The $R_{o,max}$ value of the main coals in the region varies from 0.7-1.1% (Bao, 2019).

The Tucheng block (TU) is an N-W trending syncline in north Panxian county (Figure 1D) (Wu et al., 2016). Approximately 50 coal strata are present within the Longtan Formation. The block has experienced a history similar to the Qingshan block (Wu et al., 2016). The coals experienced lower maximum burial depth at the end of mid-Jurassic (< 4 km) and a reduced thermal effect during Yanshanian orogeny where the maximum reservoir temperature attained 140°C. Basin inversions occurred during the Yanshanian orogeny and in Cenozoic. The $R_{o,max}$ values are about 1.0-1.3% (Gui, 1999; Dou, 2012).

The Yangmeishu syncline block (YA) is about 350 km^2 (Figure 1C) (Shan et al., 2018). There are 47-78 coal seams with a total thickness of 45 m within the Longtan Formation. The thermal history of the Yangmeishu block is currently unknown. Based on the $R_{o,max}$ values (1.5-1.9%; Shan et al. (2018)), the maximum burial depth of the coal seam is assumed between TU and QI blocks.

3. Sampling and analysis

Ten CBM samples were collected in April 2018 from the four blocks identified in Figure 1; Dahebian (n=2), Yangmeishu (2), Tucheng (3) and Qingshan (3). All gases are from oblique wells that extract methane from three or more coal seams. The number and layers of coal seams exploited in each block are different. Although the sampling sites are in close proximity within each block, the oblique drilling means the distance of subsurface coal seams between any two wells is more than 200 m. Well depths range from 740 to 1200 m (Table 1). The sampling wells have produced gas for over 1 to 37 months.

Samples were collected and stored in Cu tubes at 1.5-2 bar using the method described in Györe et al. (2015). Approximately 50% of the gas in each tube was used for the determination of the major gas composition and stable isotopes. Major gas composition was determined in ten samples using a Hewlett Packard 5890 gas chromatograph (GC) in SUERC. The uncertainty (1σ) of gas abundance is ± 0.3%. The methane carbon isotopic composition ($\delta^{13}C_{CH4}$) was determined using a VG SIRA II dual inlet isotope ratio mass spectrometer (Dunbar et al., 2016) using established procedures in Györe et al. (2018). $\delta^{13}C_{CH4}$ values were determined relative to PDB (Craig, 1957). The hydrogen isotope composition of the methane (δD_{CH4}) was analysed using a VG Optima dual inlet isotope ratio mass spectrometer (Donnelly et al., 2001). δD_{CH4} values were determined relative to V-SMOW (Gonfiantini, 1978). Experimental uncertainties at 1σ level of $\delta^{13}C_{CH4}$ and δD_{CH4} values are ±0.3‰ and ±3‰, respectively.

The remaining gas was used for the analysis of noble gas isotopes using a MAP 215-50 mass spectrometer following the procedures described in Györe et al. (2015, 2017). Blank levels for all isotopes were negligible. The mass spectrometer sensitivity and mass fractionation factors were determined using the HESJ standard for He (Mishima et al., 2018), and air for Ne, Ar, Kr and Xe. The reproducibility of the absolute concentrations is <3% in all cases, and the reproducibility of isotopic ratios is less than 1%.

4. Results

Methane (>90%) is the dominant content in all samples (Table 1). The DA gases have the lowest methane (90.3-92.9%) and CO_2 (≤0.1%) and the highest wet gas ($C_2H_6 + C_3H_8$, >2%) concentrations. The QI and YA gases have higher methane (>96%) and CO_2 (0.2-1.2%) and lower wet gas concentrations. CH_4/CO_2 ratios vary from 80 to 950, and $CH_4/(C_2H_6 + C_3H_8)$ ratios from 16 to 971. The carbon and hydrogen isotopic compositions of the methane range from -41.6 to -34.9‰ and -185 to -140 ‰, respectively (Table 4.1). The QI and YA gases ($\delta^{13}C_{CH4}$ = -36.6 to -34.9‰ and δD_{CH4}= -158 to -140‰) are isotopically heavier than the DA and TU gases ($\delta^{13}C_{CH4}$ = -41.6 to -39.9 ‰ and δD_{CH4}= -185 to -160‰).

The concentration and isotopic composition of noble gases are listed in Table 2. ^4He concentrations range from 41 to 1,136 ppmv while $^3He/^4He$ ratios vary from 0.005 to 0.025 R_A, where R_A is the atmospheric ratio of 1.34×10^{-6} (Mishima et al., 2018). The variation in $^3He/^4He$ shows no clear correlation with ^4He abundance. ^4He concentrations and $^3He/^4He$ of gases in each block are relatively uniform. Helium concentrations generally decrease as the maturity of

coal increases. For example, the QI gases from the most mature coals have the lowest ^{4}He concentration (41-68 ppmv). ^{20}Ne concentrations range from 0.004 to 0.043 ppmv. $^{20}Ne/^{22}Ne$ and $^{21}Ne/^{22}Ne$ vary from 9.68 ± 0.03 to 9.84 ± 0.05 and from 0.0308 ± 0.0005 to 0.0436 ± 0.0008, respectively. Although $^{20}Ne/^{22}Ne$ overlap the air value (9.80 ± 0.08), $^{21}Ne/^{22}Ne$ are distinctly higher than air (0.0290 ± 0.0003). ^{40}Ar concentrations range from 4 to 41 ppmv. The especially low ^{40}Ar concentrations (4-7 ppm) are present in YA gases. $^{40}Ar/^{36}Ar$ range from 454 ± 3 to 647 ± 6, significantly higher than air value (298.5) showing no trend with ^{40}Ar or ^{36}Ar concentrations. $^{38}Ar/^{36}Ar$ are indistinguishable from air. ^{84}Kr and ^{132}Xe concentrations range from 1.7-18.8 $\times 10^{-4}$ ppmv and 1.3-9.2 $\times 10^{-5}$ ppmv, respectively.

5. Discussion

5.1. The origin of CBM in LPC

The relative abundances of the major gases and the stable isotopic composition of the LPC methane in each block are broadly consistent (Table 1). This implies that the CBM within each block has a similar origin. The $C_1/(C_2+C_3)$ ratios and stable isotopic composition of methane ($\delta^{13}C_{CH4}$ and δD_{CH4}) in samples plot within the thermogenic field and secondary microbial methane fields (Figure 4). The addition of microbial methane would increase $C_1/(C_2+C_3)$ ratios and generate more negative $\delta^{13}C_{CH4}$ (Vinson et al., 2017). A weak positive relationship between $C_1/(C_2+C_3)$ ratio and $\delta^{13}C_{CH4}$ in LPC CBM tends to rule this out (Figure 4A). Preferential dissolution of $^{13}CH_4$ in groundwater can also explain the variation in CBM isotope compositions (Qin et al., 2006). However, experimental work demonstrates that only a small depletion of $\delta^{13}C$ (<-0.5‰) coincides with significant enrichment of δD (<16‰) in the free methane phase (Bacsik et al., 2002). This is opposite to the consistently increasing trend and smaller than the observed changes in $\delta^{13}C_{CH4}$-δD_{CH4} data (Figure 4B).

$C_1/(C_2+C_3)$, $\delta^{13}C_{CH4}$ and δD_{CH4} appear to increase coherently with coal maturity ($R_{o,max}$) (Table 1, Figure 5), implying that the variation of major gas components and stable isotopic values of methane across the LPC is related to the extent of coalification. Thermogenic methane released from coals becomes enriched in ^{13}C and ^{2}H as the coalification process progresses (Rice, 1993; Strąpoć et al., 2011). The thermal cracking of wet gas with further maturation results in a reversal of the increase of $C_1/(C_2+C_3)$ (Burruss and Laughrey, 2010). This may go some way to explaining the positive trend between $C_1/(C_2+C_3)$ and coal maturity ($R_{o,max}$) and also the abnormally high $C_1/(C_2+C_3)$ ratio in QI gases (192-971). It is worth

noting that the C and H isotopic composition of methane in the QI gases overlap with the YA gases (Figure 5), even though $C_1/(C_2+C_3)$ and coal rank in QI block are evidently higher. It might be a result of fractionation caused by adsorption/desorption and diffusion of methane in the coals (Chen et al., 2019).

In Figure 4B, it is clear that the δD_{CH4} of the LPC gases is comparable to the gases from Qinshui Basin and Lower Silesian Basin, while $\delta^{13}C_{CH4}$ is evidently more negative. Thermogenic methane is generated by the thermal cracking of organic matter which is the main source of the hydrogen of methane (Strąpoć et al., 2006). The isotopically heavy H in the LPC methane may reflect the enriched deuterium in organic matter. The aqueous environment is also critical for δD_{CH4} as the high-temperature exchange of hydrogen between methane and organic matter with formation water cannot be neglected (Strąpoć et al., 2006). The hydrogen isotope composition of formation water in LPC is -50 to -25‰ (Wu et al., 2018). While the stable isotopes of water in the Lower Silesian Basin is not available, the δD_{CH4} of coal waters from the Qinshui basin (-82 to -38‰, mainly < -60‰; Zhang et al. (2018)) is significantly lower than LPC. Thus, the exchange with isotopically heavier hydrogen from the formation water might also influence the LPC methane δD composition.

5.2 The accumulation of radiogenic noble gases

The low $^3He/^4He$ (0.005 to 0.025 R_A) of the LPC gases are consistent with a radiogenic origin for the He. The QI gases $^3He/^4He$ (0.017 to 0.025 R_A) are systematically higher than recorded by the other three fields (0.005 to 0.013 R_A). The high $^4He/^{20}Ne$ ratios (2,554-31,784) exclude a discernible contribution of air-derived He (Figure 6). Radiogenic production of ^4He occurs mostly by U and Th decay (Morrison and Pine, 1955). The production of ^3He in crustal rocks is dominantly nucleogenic, from the reaction $^6Li(n,\alpha)^3H(\beta^-)^3He$ (Morrison and Pine, 1955) and is largely dependent on the concentration of Li and the abundance of large neutron cross-section elements (B, Be, Nd, Gd, etc.). Using the range of Li concentration (9-105 ppm) and the average concentration of the large neutron cross-section elements in the Liupanshui coals (Li, 2015; Zhuang et al., 2000), we calculate that the $^3He/^4He$ produced in the coals ranges from 0.008 to 0.093 R_A. This covers the majority of the values measured in the Liupanshui CBM gases. The extremely low $^3He/^4He$ ratios in DA and YA gases (0.005-0.007 R_A) might be due to local variation in the concentration of Li and the large neutron cross-section elements.

The Ne isotope composition of the LPC gases (Figure 7A) requires a significant contribution of nucleogenic Ne in addition to air. The YA, DA and TU gas data fall in a triangle defined by air, average crust ($^{20}Ne/^{22}Ne$ = 0, $^{21}Ne/^{22}Ne$ = 0.47; Kennedy et al. (1990)) and one or more components with higher $^{20}Ne/^{22}Ne$ for given $^{21}Ne/^{22}Ne$. If the Ne is mantle-derived ($^{20}Ne/^{22}Ne$ = 12.5, $^{21}Ne/^{22}Ne$ = 0.06; Ballentine et al. (2005)), the sample with the highest $^{20}Ne/^{22}Ne$ (QSC, 9.84 ± 0.05) would contain 17% mantle-derived Ne. However the presence of mantle-derived Ne is inconsistent with the absence of mantle ^{3}He in the LPC gases.

The Ne isotope data are more likely explained by the presence of nucleogenic Ne that is produced with a higher $^{20}Ne/^{22}Ne$ than the average crustal value. Neon isotopes are mainly produced in the crust by alpha-particle reactions on O ($^{17,18}O(\alpha,n)^{20,21}Ne$) and F ($^{19}F(\alpha,n)^{22}Na(\beta^{+})^{22}Ne$) (Wetherill, 1954). Consequently, variation in the $^{20}Ne/^{22}Ne$ and $^{21}Ne/^{22}Ne$ of crustal gases is dependent on the O/F ratio near (< 20 μm) U and Th-derived α particles (Kennedy et al., 1990). Assuming an oxygen concentration of 10% based on the concentration of major oxides and an average F concentration of 42 ppm (Li, 2015), the O/F ratio in LPC coals is ~2,400. This would result in $^{20}Ne/^{22}Ne$ and $^{21}Ne/^{22}Ne$ production ratios of 1.1 and 11.4, respectively, which is a better fit for the data than the average crustal value.

An alternative explanation is that Ne in LPC is mainly from the Archaean crust. There is increasing evidence that the Archaean crust has generated Ne with a $^{20}Ne/^{22}Ne$ and $^{21}Ne/^{22}Ne$ that are higher than Phanerozoic crust because of the low fluorine abundance (Holland et al., 2013; Lippmann-Pipke et al., 2011). The LPC is located in the western part of the Yangtze block and is likely underlain by Archaean basement (Wang et al., 2012; Zheng et al., 2006). It is possible that the Ne in LPC originated from the Archaean crust, from the diffusion of a crustal flux of Ne and/or advecting up the extensive network of deep faults (Zhang, 2017).

As with Ne isotopes, the $^{21}Ne/^{22}Ne$-$^{40}Ar/^{36}Ar$ compositions of the YA, DA and TU gases fall on a broad linear trend that is consistent with mixing between air and one or more crustal gases that have variable concentrations of nucleogenic ^{21}Ne and ^{22}Ne, and radiogenic ^{40}Ar (Figure 7B). The QI gases define a mixing relationship between air and deep gas with distinctly lower $^{21}Ne/^{22}Ne$ yet similar $^{40}Ar/^{36}Ar$ compared with the other three blocks. The concentrations of radiogenic ^{40}Ar (denoted as $^{40}Ar^{*}$ and calculated by removing atmospheric ^{40}Ar and assuming negligible magmatic $^{40}Ar^{*}$) and nucleogenic ^{21}Ne (denoted as $^{21}Ne^{*}$ and calculated in the same way as $^{40}Ar^{*}$) are listed in Table 3. $^{4}He/^{40}Ar^{*}$ and $^{21}Ne^{*}/^{40}Ar^{*}$ in LPC CBM span wide ranges, 4-66 and 0.27-3.0×10^{-6}, respectively (Table 3). Taking the average U (5.2 ppm), Th (4.6 ppm), K (0.3%), Mg (0.1%) and O (10%) concentrations values in local coals (Li, 2015), the in-situ

production rates of ^{4}He, $^{21}Ne^{*}$ and $^{40}Ar^{*}$ can be estimated (Ballentine and Burnard, 2002). The predicted ratios of $^{4}He/^{40}Ar^{*}$ and $^{21}Ne^{*}/^{40}Ar^{*}$ are 67 and 7.5×10^{-7}, respectively. The $^{4}He/^{40}Ar^{*}$ of the TU, DA and YA gases are comparable and slightly lower to the predicted in-situ ratio but significantly higher than the average crustal value (~5, Ballentine and Burnard (2002)), while $^{21}Ne^{*}/^{40}Ar^{*}$ are higher than predicted values and also the average crustal value (~2.9×10^{-7}, Ballentine and Burnard (2002)) (Figure 8). The $^{4}He/^{40}Ar^{*}$ and $^{21}Ne^{*}/^{40}Ar^{*}$ in QI gases, in contrast, are both lower than the in-situ generation rate, albeit comparable with the average crustal values.

The elevated $^{21}Ne^{*}/^{40}Ar^{*}$ in most LPC coals likely reflects the addition of $^{21}Ne^{*}$ that originated outside the coals. However, $^{4}He/^{40}Ar^{*}$ ratios are not supportive of excess ^{4}He, despite the mobility of He in the shallow crust (Jähne et al., 1987). The decoupling of $^{4}He/^{40}Ar^{*}$ from $^{21}Ne^{*}/^{40}Ar^{*}$ indicates a preferential escape of He from the coals. QI gases have lower $^{4}He/^{40}Ar^{*}$ and $^{21}Ne^{*}/^{40}Ar^{*}$ than other blocks and the predicted values, which suggests a greater He and Ne loss. In order to explain the lower $^{21}Ne/^{22}Ne$ but rather constant $^{40}Ar/^{36}Ar$ in QI gases (Figure 7B), the Ne loss must have occurred before the addition of air-derived noble gases that are likely from groundwater. The diffusive loss of Ne from gas reservoirs can result in isotopic fractionation (Bourg and Sposito, 2008). In this case, it will leave isotopically heavy Ne in the reservoir, consistent with Ne isotope composition of the QI gases which have lower $^{20}Ne/^{22}Ne$ than air (Figure 7A).

It can be inferred that the gas escape is a result of basin exhumation (Dou, 2012). $^{4}He/^{40}Ar^{*}$ and $^{21}Ne^{*}/^{40}Ar^{*}$ decrease coherently with the increasing maturity of coals. The QI block has experienced the most intensive and recent basin inversion (Dou, 2012), thus it is reasonable to expect that the block has lost most He and Ne and not regained significant radiogenic He and Ne after basin inversion. Han et al. (2010) has proved the weak sorption of Ar in high mature coals. The adsorption capacity of coals generally increases with maturity (Moore, 2012). High-maturity coals theoretically have stronger adsorption capacity and may retain more Ar than lower rank coals. It results in a similar $^{40}Ar^{*}$ concentration in LPC gases but variable ^{4}He and $^{21}Ne^{*}$ and consequently the lowest $^{4}He/^{40}Ar^{*}$ and $^{21}Ne^{*}/^{40}Ar^{*}$ ratios in QI gases. Assuming the highest $^{4}He/^{40}Ar^{*}$ and $^{21}Ne^{*}/^{40}Ar^{*}$ in DA gases as the initial values, more than 96% of ^{4}He and 91% of $^{21}Ne^{*}$ have lost from QI gases compared with Ar.

5.3 The accumulation of air-derived noble gases

^{20}Ne, ^{36}Ar, ^{84}Kr and ^{132}Xe in natural gases are mainly derived from air, typically entering reservoirs dissolved in groundwater (Ballentine et al., 2002). Air-saturated water (ASW) in the LPC region, equilibrated with air at 15°C in an altitude of 1500 m and containing 10% Ne excess air composition, has $^{20}Ne/^{36}Ar = 0.16$, $^{84}Kr/^{36}Ar = 0.039$ and $^{132}Xe/^{36}Ar = 0.0026$ (Kipfer et al., 2002). The LPC CBM yields $^{20}Ne/^{36}Ar$ (0.23-0.70) that are significantly higher than the local ASW, while $^{84}Kr/^{36}Ar$ (0.010-0.025) and $^{132}Xe/^{36}Ar$ (0.0002-0.0012) in all samples except QSC are below the ASW values (Figure 9). Most samples have $^{20}Ne/^{36}Ar$ that is higher than the air value (0.53), and $^{84}Kr/^{36}Ar$ and $^{132}Xe/^{36}Ar$ that are lower than the air values (0.021 and 0.0007, respectively). Thus, the relative enrichment of Ne and depletion of Kr and Xe cannot be explained by simple mixing with air-derived noble gases (Figure 9). Elemental fractionation occurs in response to solubility-related partitioning between different reservoir fluids (e.g., Ballentine et al., 2002; Ballentine et al., 1991; Battani et al., 2000; Gilfillan et al., 2008). As no oil is present in this system, partitioning is likely only between free gas and water. The solubility-controlled fractionation factors of noble gases in LPC reservoir groundwater at 45°C and 9.9 MPa, and salinity of 0.15 mol/L (Wu et al., 2018), are $K_{Ne}/K_{Ar} = 2.3$, $K_{Kr}/K_{Ar} = 0.67$ and $K_{Xe}/K_{Ar} = 0.49$, calculated from Henry's constants of noble gas and corrected from liquid-phase activity coefficients and gas-phase fugacity coefficients (Ballentine et al., 2002; Crovetto et al., 1982; Smith and Kennedy, 1983). The maximum $^{20}Ne/^{36}Ar$ ratio that the gas phase can obtain by closed-system (batch) or open-system (Rayleigh) fractionation is 0.38 (Figure 9). This cannot explain the measured $^{20}Ne/^{36}Ar$ of the DA, TU and YA gases (0.56-0.70). More air bubble dissolution in groundwater can increase the initial $^{20}Ne/^{36}Ar$ in ASW and thus the maximum fractionated $^{20}Ne/^{36}Ar$ from water to gas phase (Battani et al., 2000; Heaton and Vogel, 1981). However the high excess air is uncommon in humid monsoon climates such as in southern China, thus it is an unlikely explanation.

Enrichments of ^{20}Ne and depletions of ^{84}Kr was observed in CBM from the Illinois Basin (Moore et al., 2018). It is explained by a dual-phase (free gas + brine) migration of exogenous super-saturated hydrocarbon gas-rich brines from the underlying source rocks, during which the elevated $^{20}Ne/^{36}Ar$ ratio develops in the free gas phase based on different solubilities (Darrah et al., 2015; Darrah et al., 2014; Moore et al., 2018). A systematic variance between air-derived noble gases with $C_1/(C_2+C_3)$ and $\delta^{13}C_{CH4}$ was also generated during the process as hydrocarbon gas from the underlying source rocks is the main carrier gas. This mechanism might have operated in LPC, where the underlying shales supply hydrocarbon-rich fluids

(Zhang, 2017). However the absence of correlation between $^{20}Ne/^{36}Ar$ and $\delta^{13}C$, $C_1/(C_2+C_3)$ in LPC gases (Table 1 and 2) appears to rule out an externally-sourced hydrocarbon-charged brine in the LPC.

^{20}Ne enrichments can be caused by the re-dissolution of gases exsolved from groundwater in CO_2-rich systems (Gilfillan et al., 2008; Zhou et al., 2012). Gas bubbles generated by CO_2 injected into groundwater strip the dissolved noble gases and accumulate in a gas cap. The redissolution into the gas-stripped groundwater once CO_2 filling ceases follows the Rayleigh fractionation law if the groundwater continuously migrates relatively to the gas phase (Gilfillan et al., 2008; Zhou et al., 2012). In the case of LPC effervescence and then re-dissolution of CBM in response to the continuous or episodic drops in reservoir pressure (and temperature) during basin inversion since the Late Jurassic (Dou, 2012) may have driven the exsolution process. Over 170 Myr the coals in the DA block have likely uplifted from 3,800 m to 1,000 m depth (Dou, 2012). Assuming that the reservoir pressure was equal to the hydrostatic pressure and the average methane proportion remained at 92% during basin inversion, methane solubility in the formation water decreased from 0.0016 to 0.006 cm^3/cm^3 (Ballentine et al., 2002; Tishchenko et al., 2005). Consequently, the formation water would have become over-saturated with respect to the dissolved methane, resulting in the generation of methane bubbles which would have stripped the dissolved noble gases from the water. Methane bubble generation will cease with the cessation of basin inversion and the gas-phase noble gases can re-dissolve into the degassed groundwater. The process is modelled as an open system Rayleigh fractionation under LPC reservoir conditions and could explain the high $^{20}Ne/^{36}Ar$ ratios (Figure 9).

In ^{20}Ne-^{36}Ar-^{84}Kr plot, only gas from the YMC well plots on fractionation line expected if the formation water started with an ASW noble gas composition (Figure 9A). With the exception of the two QI gases, all samples plot above the water-gas fractionation lines in ^{20}Ne-^{36}Ar-^{84}Kr and ^{20}Ne-^{36}Ar-^{132}Xe space (Figure 9). Variable $^{84}Kr/^{36}Ar$ and $^{132}Xe/^{36}Ar$ with the narrow range of $^{20}Ne/^{36}Ar$ suggest that relative abundances of heavy gases are not only controlled by the re-dissolution fractionation process. An excess of ^{84}Kr of up to 280%, and a 1300% excess of ^{132}Xe, over the modelled values are required to explain the range of $^{84}Kr/^{36}Ar$ and $^{132}Xe/^{36}Ar$ ratios. Most samples plot below the ASW fractionation line in ^{36}Ar-^{84}Kr-^{132}Xe space, except for one TU and QSC gas (Figure 10), indicating that the majority of the gases appear to contain excess ^{132}Xe relative to ^{84}Kr. A 200% excess of Xe relative to Kr is required to explain the $^{132}Xe/^{36}Ar$ values.

Xe and Kr excesses are frequently recorded by CBM (McKavney, 2019; Zhou et al., 2005). The relative enrichment pattern (Xe > Kr > Ar) is consistent with the decreasing atomic radius and expected adsorption on organic matter or trapped in the coal matrix (Torgersen et al., 2004). Xe and Kr are desorbed from the coals due to the de-pressure and extracted out with methane during the gas extraction process, resulting in the enrichment of Xe and Kr in the produced gas. This could be the case in LPC gases. The lower $^{84}Kr/^{36}Ar$ and $^{132}Xe/^{36}Ar$ than predicted in the two QI gases may reflect stronger adsorption onto local high maturity coals. The strong adsorption capacity causes the failure of desorption of trapped gases and also retention of ASW-derived Xe and Kr in groundwater, as noted for Southeast Qinshui Basin (Chen, 2021).

5.4 Effect of basin inversion on retention of methane

The He-Ne-Ar isotopes of the LPC methane samples clearly identify varying degrees of loss of free gas during basin inversion. Methane is generally present as free gas in the pores of coals and adsorbed to the surface of coals (Moore, 2012). The noble gases strongly imply that free methane was lost, thus it is pertinent to evaluate the impact of this gas loss on methane retention. In the model of Xia and Tang (2012) methane loss is mainly governed by the change of temperature and pressure of the reservoir during basin inversion, the coal porosity and density, the proportion of total organic carbon (TOC) in the coals, the heat of adsorption and standard entropy of adsorption of methane in coals for free and adsorbed gas loss. The model estimates the free gas content before and after basin inversion assuming the Peng-Robinson equation of state and the change of adsorbed gas content following the Langmuir equation. DA and QI blocks have experienced the most and least intensive basin inversion respectively, thus the methane loss from these two blocks provides upper and lower limits. As no TOC data of LPC coals are available, we assume 70% for all four blocks; this is similar to the Qinshui Basin coals (Yin et al., 2016). The coal density is taking 1.5 g/cm^3 (Shan et al., 2018). Standard entropy of adsorption of methane in coals is -76 J/(K mol) following Xia and Tang (2012).

The modelled results for the DA (2,500 m basin inversion) and QI blocks (4,200 m inversion) are shown in Table 4. The QI block is estimated to have lost 77% of the free methane, while the amount of adsorbed methane has slightly increased during basin inversion. The DA block has lost less free gas as a consequence of the less intensive basin inversion, and a slight adsorbed methane loss due to the lower adsorption capacity. The amount of adsorbed methane in the two blocks is relatively stable before and after gas loss and significantly

higher than that of free gas at the current burial depth. It underlines the importance of the coal adsorption capacity on methane retention. The small difference (6%) in total methane loss indicates that the extent of methane loss from these four blocks is likely similar. However, this assumes the same TOC and standard entropy of adsorption for all four blocks. The evident variation in coal maturity ($R_{o,max}$ from 0.7 to 3%) implies that this might not be the case. These two parameters reflect the adsorption capacity of coals (Xia and Tang, 2012; Wang et al., 2018). The adsorption capacity of coals generally increases with maturity (Moore, 2012). The lower adsorption capacity in DA block implies that more adsorbed gas was lost during basin inversion. This is broadly consistent with the gas contents measured in the fields; QI block (~13 m^3/t, Lei et al., 2012) and YA block (~16 m^3/t, Shan et al., 2018) is higher than DA block (~7-10.9 m^3/t, Bao 2019) and TU block (~8.6 m^3/t, Zhang 2019).

This model does not consider the role of groundwater, which is important in methane storage and production in coals (Moore, 2012). It might explain why the QI block has lower gas content than YA block. An interesting observation is that the practical gas production rate in QI wells (100-300 m^3/day) is the lowest in four blocks (300-400 m^3/day for TU, 2000-5000 m^3/day for YA, 400-600 m^3/day for DA). The prediction of the volume of groundwater to gas ratio (V_w/V_g) provides an opportunity to assess the role of groundwater on both gas preservation and production. The V_w/V_g in the two stages of the fractionation process can be calculated following Gilfillan et al. (2008) and is shown in Table 5. The proportion of ^{36}Ar lost from the gas phase into solution during the open system re-dissolution process is estimated from the measured $^{20}Ne/^{36}Ar$ ratios in gas phase. The volume of groundwater that has interacted with gas during the re-dissolution process could then be calculated and present as stage2 V_w/V_g. The initial concentration of ^{36}Ar in gas phase before the re-dissolution fractionation is easily recovered with measured ^{36}Ar concentration and the proportion of ^{36}Ar re-dissolved in groundwater. Combining the concentration of ^{36}Ar in ASW from LPC, the volume of groundwater that noble gases have been stripped out to supply ^{36}Ar in gas phase could be evaluated. The volumetric ratio of groundwater to gas in gas stripping stage is present as stage1 V_w/V_g. The detailed calculation is present in the Appendix.

The calculated stage 1 V_w/V_g (0.08-0.79 in STP) has a weak negative trend with coal maturity in DA, TU and YA blocks (Table 1 and 5). The porosity of coals generally decreases from the start of coalification as macro-pores are destroyed by compaction, while this reverses during the change from low-volatile bituminous coals to anthracite due to the development of micropores (İnan et al., 2018; Levine, 1993). The DA block coals have a lower gas content but

higher porosity, leaving the stage 1 V_w/V_g reasonably the highest in four blocks. The gas content and porosity in QI block are both higher and could explain that the stage 1 V_w/V_g (0.11-0.29) is not the lowest. The low porosity and permeability likely indicate a stagnant reservoir condition and could have benefited the retention of free gas during gas loss. From these simple observations, it appears, counter-intuitively, that YA block should have retained most of the primary methane reserve. Although DA coals have had the most open system in this stage (stage1 V_w/V_g = 0.68-0.79), the basin inversion of this block is weaker. The loss of free gas is expected to be lower.

The stage2 V_w/V_g (0.29-1.18 in STP) are higher than stage1 V_w/V_g in four blocks. More groundwater has interacted with gas in the re-dissolution process. This might indicate that the reservoir condition of local coals has changed into higher permeability and porosity at the shallow depth where allows a stronger groundwater flow. Dewatering would cause the effective pressure drop in the reservoir and desorption of gas. The higher permeability and porosity also would improve the gas extraction. The stage2 V_w/V_g in YA block has seen the most significant increase. It is consistent with the high gas production rate in this block. In contrast, the stage2 V_w/V_g in two QI samples remains low. This suggests a relatively low permeable and porous coefficient for reservoir fluids in the coal beds before gas extraction. The dewatering then would not efficiently cause the desorption of methane and also heavy noble gases in the reservoir. It is consistent with the low gas production rate and the lower $^{84}Kr/^{36}Ar$ and $^{132}Xe/^{36}Ar$ than predicted values in these two QI samples.

6. Conclusion

This study presents noble gas isotope and traditional major gas, stable isotope data for the coalbed methane samples from Liupanshui Coalfield. Several important conclusions have been reached:

- The methane is thermogenic in origin without a significant contribution of microbial methane. The compositional variability between four blocks is mainly controlled by the different maturation extent of coals in each block.
- Noble gases reveal a mixture of air-derived gases from groundwater (ASW) with in-situ generated gases in the reservoir. The enrichment of light Ne isotopes relative to the general air-crust mixing line implies the likely source of *in situ* Ne from local (F-poor) coals.

- The radiogenic noble gases reveal a gas loss event during which He and Ne are preferential to loss compared with Ar, and subsequent addition of air-derived noble gases (e.g. ^{20}Ne, ^{36}Ar). In high mature coals, mass fractionation has also been observed. The gas diffusion reached 96% He and 91% $^{21}Ne^{*}$ discrepancy compared to Ar.

- Gas stripping and re-dissolution fractionation processes are required to explain the extremely high $^{20}Ne/^{36}Ar$ of the gases. The high Kr/Ar and Xe/Ar observed in most gases are explained by the desorption of initial trapped Xe and Kr from the coal matrix. Locally high maturity coals in the QI block show strong adsorption capacity for Xe and Kr, resulting in the lower $^{84}Kr/^{36}Ar$ and $^{132}Xe/^{36}Ar$ than modelled for produced CBM.

- Modelling the methane loss and the volume of groundwater that gas has interacted with during basin inversion suggests a promising high gas reserve and gas production from the high mature coals that have seen the least amount of groundwater in the gas stripping stage (basin inversion) and the highest amount of groundwater in the re-dissolution process (shallow depth). This is consistent with the gas content and gas production rate data in the field.

CRediT authorship contribution statement

BC, FS and SX conceived the study. BC wrote the first draft of the manuscript. All co-authors assisted writing and editing. BC and SX collected the samples. BC performed all laboratory analyses. BC performed data interpretation, with help from FS, DG and SX. FS, SX and CL supported funding, supervision and measurement capabilities.

Competing interest

The Authors declare no conflict of interest.

Acknowledgements

The research is part of BC's PhD at SUERC. It was funded by University of Glasgow, Total E&P and Tianjin University. We are grateful to Liupanshui Energy Investment Development Co. Ltd. for permission to collect samples and especially Yanlong Li for the assistance on-site and providing relevant information. We appreciate the assistance that Dr Marta Zurakowska and Mr Terry Donnelly have supported in the laboratories.

Appendix: Calculation of the volume of groundwater that has interacted with gas phase based on the re-dissolution model

Gilfillan et al. (2008) proposed a re-dissolution model to explain the unexpectedly high $^{20}Ne/^{36}Ne$ in CO_2-dominated gases that had not seen oil phase. The re-dissolution model is now widely used (Zhou et al., 2012; Darrah et al., 2014; Moore et al., 2018). It describes two-stage fractionation. In the first stage oversaturated gas bubbles generated in the water phase strip the dissolved noble gases and accumulate in a gas cap. The gas-phase noble gases retain their original ASW-like abundance pattern. As they redissolve into the gas-poor groundwater they are subject to the Rayleigh fractionation law if the groundwater continuously migrates relatively to the gas phase:

$$(\frac{^{20}Ne}{^{36}Ar})_g = (\frac{^{20}Ne}{^{36}Ar})_o f^{(\alpha-1)} \qquad (1)$$

where $(\frac{^{20}Ne}{^{36}Ar})_g$ is the measured ratio in gas samples, $(\frac{^{20}Ne}{^{36}Ar})_o$ is the initial ASW $^{20}Ne/^{36}Ar$ (0.16, see section 5.3) in the gas phase, and f is the proportion of ^{36}Ar retained in the gas. α is the fractionation factor from liquid to gas phase:

$$\alpha = 1/(\frac{\frac{\gamma_{Ne}}{\Phi_{Ne}} K_{Ne}^{groundwater}}{\frac{\gamma_{Ar}}{\Phi_{Ar}} K_{Ar}^{groundwater}}) \qquad (2)$$

where K is Henry's constants for noble gases in water, γ is the liquid phase activity coefficient, ϕ is gas phase fugacity coefficient (see section 5.3). The proportion of ^{36}Ar (1- f) lost from the gas phase into solution during the open system re-dissolution process is thus estimated from the measured $^{20}Ne/^{36}Ar$ ratios in the gas phase. In this process, assuming gas phase continuously interacts with an extremely small amount of groundwater ($(V_w/V_g)_o \rightarrow 0$ at each dissolution stage), the partition of noble gases reaches equilibrium in each dissolution stage. The amount of ^{36}Ar retained in the gas phase could be estimated (Ballentine et al., 2002):

$$\frac{[^{36}Ar]_{g,o}}{[^{36}Ar]_t} = (\frac{22400 T \rho_W}{1000 \times 273 \frac{\gamma_{Ar}}{\Phi_{Ar}} K_{Ar}^m} \times (\frac{V_W}{V_g})_0 + 1)^{-1} \qquad (3)$$

where $[^{36}Ar]_{g,o}$ is the number of moles of ^{36}Ar in gas phase in each dissolution stage and $[^{36}Ar]_t$ is the present total number of moles. When $(V_w/V_g)_o$ is close to 0, $[^{36}Ar]_{g,o}$ is close to

546 $[^{36}Ar]_t$. T is the temperature (K) in the reservoir, ρ_W is the porosity of the liquid, $K_{Ar}{}^m$ is
547 Henry's constant in the unit of Kg atm/mol. The iterative times (d) that a small volume of
548 gas-poor groundwater interacts with gas phase in the second-stage fractionation could then be
549 calculated:

550 $$d = \frac{LN(f)}{LN(\frac{[^{36}Ar]_{g,o}}{[^{36}Ar]_t})} \qquad (4)$$

551 The volumetric ratio of groundwater to gas in this stage is present as stage2 V_w/V_g. Stage2
552 V_w/V_g at standard condition (STP) could be estimated as follows:

553 $$stage2\ V_w/V_g = \frac{dTP_0}{T_0P}(\frac{V_W}{V_g})_0 \qquad (5)$$

554 where T_0 and P_0 are the temperature (K) and pressure (atm) at standard condition (1atm, 273
555 K). P is the pressure (atm) in the reservoir.

556 For the gas stripping stage, the volume of groundwater that noble gases have been stripped
557 out to supply ^{36}Ar in the gas phase can be evaluated based on the proportion of ^{36}Ar retained
558 in gas phase and the predicted concentration of ^{36}Ar in air-saturated water from LPC region.
559 The initial concentration of ^{36}Ar (C_{Ar}^i) in the gas phase before the re-dissolution fractionation
560 is recovered with measured ^{36}Ar (C_{Ar}^g) concentration and the proportion of ^{36}Ar retained in
561 gas phase (f):

562 $$C_{Ar}^i = \frac{C_{Ar}^g}{f} \qquad (6)$$

563 The concentration of ^{36}Ar (C_{Ar}^0) in air-saturated water from LPC region is calculated to be
564 9.9×10^{-7} cm^3STP/cm^3 H_2O following Kipfer et al. (2002). The volumetric ratio of water to
565 gas in the gas stripping stage (stage 1 V_w/V_g) is calculated as follows:

566 $$stage1\ V_w/V_g = \frac{C_{Ar}^i}{C_{Ar}^0} \qquad (7)$$

References

Aravena, R., Harrison, S.M., Barker, J.F., Abercrombie, H., Rudolph, D., 2003. Origin of methane in the Elk Valley coalfield, southeastern British Columbia, Canada. Chem. Geol., 195(1–4): 219-227.

Bacsik, Z., Lopes, J.N.C., Gomes, M.F.C., Jancsó, G., Mink, J., Pádua, A.A.H., 2002. Solubility isotope effects in aqueous solutions of methane. The Journal of Chemical Physics, 116(24): 10816-10824.

Ballentine, C.J., Burgess, R., Marty, B., 2002. Tracing Fluid Origin, Transport and Interaction in the Crust. In: Porcelli, D., Ballentine, C.J., Wieler, R. (Eds.), Rev. Mineral. Geochem., pp. 539-614.

Ballentine, C.J., Burnard, P.G., 2002. Production, Release and Transport of Noble Gases in the Continental Crust. In: Porcelli, D., Ballentine, C.J., Wieler, R. (Eds.), Rev. Mineral. Geochem., pp. 481-538.

Ballentine, C.J., Marty, B., Sherwood Lollar, B., Cassidy, M., 2005. Neon isotopes constrain convection and volatile origin in the Earth's mantle. Nature, 433(7021): 33-38.

Ballentine, C.J., O'Nions, R.K., Oxburgh, E.R., Horvath, F., Deak, J., 1991. Rare gas constraints on hydrocarbon accumulation, crustal degassing and groundwater flow in the Pannonian Basin. Earth Planet. Sci. Lett., 105(1): 229-246.

Bao, Q., 2019. Coalbed Methane System and Its Geological Controls in Dahebian Syncline, Guizhou, China. Master Thesis, China University of Mining and Technology, 89 pp. (In Chinese with English abstract)

Battani, A., Sarda, P., Prinzhofer, A., 2000. Basin scale natural gas source, migration and trapping traced by noble gases and major elements: the Pakistan Indus basin. Earth Planet. Sci. Lett., 181(1): 229-249.

Baublys, K.A., Hamilton, S.K., Golding, S.D., Vink, S., Esterle, J., 2015. Microbial controls on the origin and evolution of coal seam gases and production waters of the Walloon Subgroup; Surat Basin, Australia. Int. J. Coal Geol., 147-148: 85-104.

Bourg, I.C., Sposito, G., 2008. Isotopic fractionation of noble gases by diffusion in liquid water: Molecular dynamics simulations and hydrologic applications. Geochim. Cosmochim. Acta, 72(9): 2237-2247.

Burruss, R.C., Laughrey, C.D., 2010. Carbon and hydrogen isotopic reversals in deep basin gas: Evidence for limits to the stability of hydrocarbons. Org. Geochem., 41(12): 1285-1296.

Chen, B., 2021. Evolution of coalbed methane: insights from stable and noble gas isotopes. Doctoral Dissertation Thesis, University of Glasgow, 170 pp.

Chen, B., Stuart, F.M., Xu, S., Györe, D., Liu, C., 2019. Evolution of coal-bed methane in Southeast Qinshui Basin, China: Insights from stable and noble gas isotopes. Chem. Geol., 529: 119298.

Chen, X., 1995. Distribution and origin of Longtan Formation Coals in Guizhou Province. Coal Geology & Exploration 23: 21-24.

Craig, H., 1957. Isotopic standards for carbon and oxygen and correction factors for mass-spectrometric analysis of carbon dioxide. Geochim. Cosmochim. Acta, 12(1): 133-149.

Crovetto, R., Fernández-Prini, R., Japas, M.L., 1982. Solubilities of inert gases and methane in H_2O and in D_2O in the temperature range of 300 to 600 K. The Journal of Chemical Physics, 76(2): 1077-1086.

Darrah, T.H., Jackson, R.B., Vengosh, A., Warner, N.R., Whyte, C.J., Walsh, T.B., Kondash, A.J., Poreda, R.J., 2015. The evolution of Devonian hydrocarbon gases in shallow aquifers of the northern Appalachian Basin: Insights from integrating noble gas and hydrocarbon geochemistry. Geochim. Cosmochim. Acta, 170: 321-355.

Darrah, T.H., Vengosh, A., Jackson, R.B., Warner, N.R., Poreda, R.J., 2014. Noble gases identify the mechanisms of fugitive gas contamination in drinking-water wells overlying the Marcellus and Barnett Shales. Proceedings of the National Academy of Sciences, 111(39): 14076-14081.

Dawson, K.S., Strąpoć, D., Huizinga, B., Lidstrom, U., Ashby, M., Macalady, J.L., 2012. Quantitative Fluorescence *In Situ* Hybridization Analysis of Microbial Consortia from a Biogenic Gas Field in Alaska's Cook Inlet Basin. Appl. Environ. Microbiol., 78(10): 3599-3605.

Donnelly, T., Waldron, S., Tait, A., Dougans, J., Bearhop, S., 2001. Hydrogen isotope analysis of natural abundance and deuterium-enriched waters by reduction over chromium on-line to a dynamic dual inlet isotope-ratio mass spectrometer. Rapid Commun. Mass Spectrom., 15(15): 1297-1303.

Dou, X., 2012. Tectonic Evolution and Its Control on Coalbed Methane Reservoiring in Western Guizhou. Doctoral Thesis, China University of Mining and Technology, 152 pp. (In Chinese with English abstract)

Dunbar, E., Cook, G.T., Naysmith, P., Tripney, B.G., Xu, S., 2016. AMS ^{14}C Dating at the Scottish Universities Environmental Research Centre (SUERC) Radiocarbon Dating Laboratory. Radiocarbon, 58(1): 9-23.

Eberhardt, P., Eugster, O., Marti, K., 1965. A Redetermination of the Isotopic Composition of Atmospheric Neon, Zeitschrift für Naturforschung A, pp. 623.

EIA, 2010. International Energy Outlook, U.S. Energy Information Administration. www.eia.gov/oiaf/ieo/index.html.

Flores, R.M., Rice, C.A., Stricker, G.D., Warden, A., Ellis, M.S., 2008. Methanogenic pathways of coal-bed gas in the Powder River Basin, United States: The geologic factor. Int. J. Coal Geol., 76(1–2): 52-75.

Gilfillan, S.M.V., Ballentine, C.J., Holland, G., Blagburn, D., Lollar, B.S., Stevens, S., Schoell, M., Cassidy, M., 2008. The noble gas geochemistry of natural CO_2 gas reservoirs from the Colorado Plateau and Rocky Mountain provinces, USA. Geochim. Cosmochim. Acta, 72(4): 1174-1198.

Gonfiantini, R., 1978. Standards for stable isotope measurements in natural compounds. Nature, 271: 534.

Gui, B., 1999. Geological characteristics and enrichment controlling factors of coalbed methane in Liupanshui region. Acta Petrolei Sinica, 20(3): 31-37. (In Chinese with English abstract)

Györe, D., McKavney, R., Gilfillan, S.M.V., Stuart, F.M., 2018. Fingerprinting coal-derived gases from the UK. Chem. Geol., 480: 75-85.

Györe, D., Gilfillan, S.M.V., Stuart, F.M., 2017. Tracking the interaction between injected CO_2 and reservoir fluids using noble gas isotopes in an analogue of large-scale carbon capture and storage. Appl. Geochem., 78: 116-128.

Györe, D., Stuart, F.M., Gilfillan, S.M.V., Waldron, S., 2015. Tracing injected CO_2 in the Cranfield enhanced oil recovery field (MS, USA) using He, Ne and Ar isotopes. International Journal of Greenhouse Gas Control, 42: 554-561.

Györe, D., Tait, A., Hamilton, D., Stuart, F.M., 2019. The formation of NeH^+ in static vacuum mass spectrometers and re-determination of $^{21}Ne/^{20}Ne$ of air. Geochim. Cosmochim. Acta, 263: 1-12.

Han, F., Busch, A., Krooss, B.M., Liu, Z., van Wageningen, N., Yang, J., 2010. Experimental Study on Fluid Transport Processes in the Cleat and Matrix Systems of Coal. Energy Fuels, 24(12): 6653-6661.

Heaton, T.H.E., Vogel, J.C., 1981. "Excess air" in groundwater. Journal of Hydrology, 50: 201-216.

Holland, G., Lollar, B.S., Li, L., Lacrampe-Couloume, G., Slater, G.F., Ballentine, C.J., 2013. Deep fracture fluids isolated in the crust since the Precambrian era. Nature, 497(7449): 357-360.

Hosgörmez, H., 2007. Origin and secondary alteration of coalbed and adjacent rock gases in the Zonguldak Basin, western Black Sea Turkey. Geochem. J., 41(3): 201-211.

Huang, w., Qu, Z., 2021. CBM Occurrence Characteristics and Suggestions for Exploration and Development in Digua Exploration Area of Baotian Qingshan Block in Guizhou. China Coalbed Methane, 18(2): 30-35. (In Chinese with English abstract)

İnan, S., Al Badairy, H., İnan, T., Al Zahrani, A., 2018. Formation and occurrence of organic matter-hosted porosity in shales. Int. J. Coal Geol., 199: 39-51.

Jähne, B., Heinz, G., Dietrich, W., 1987. Measurement of the diffusion coefficients of sparingly soluble gases in water. Journal of Geophysical Research: Oceans, 92(C10): 10767-10776.

Ju, W., Yang, Z., Shen, Y., Yang, H., Wang, G., Zhang, X., Wang, S., 2021. Mechanism of pore pressure variation in multiple coal reservoirs, western Guizhou region, South China. Frontiers of Earth Science.

Kennedy, B.M., Hiyagon, H., Reynolds, J.H., 1990. Crustal neon: a striking uniformity. Earth Planet. Sci. Lett., 98(3): 277-286.

Kinnon, E.C.P., Golding, S.D., Boreham, C.J., Baublys, K.A., Esterle, J.S., 2010. Stable isotope and water quality analysis of coal bed methane production waters and gases from the Bowen Basin, Australia. Int. J. Coal Geol., 82(3–4): 219-231.

Kipfer, R., Aeschbach-Hertig, W., Peeters, F., Stute, M., 2002. Noble Gases in Lakes and Ground Waters. In: Porcelli, D., Ballentine, C.J., Wieler, R. (Eds.), Rev. Mineral. Geochem., pp. 615-700.

Kotarba, M.J., 2001. Composition and origin of coalbed gases in the Upper Silesian and Lublin basins, Poland. Org. Geochem., 32(1): 163-180.

Kotarba, M.J., Rice, D.D., 2001. Composition and origin of coalbed gases in the Lower Silesian basin, southwest Poland. Appl. Geochem., 16(7–8): 895-910.

Lei, B., Qin, Y., Gao, D., Fu, X., Wang, G.G.X., Zou, M., Shen, J., 2012. Vertical Diversity of Coalbed Methane Content and its Geological Controls in the Qingshan Syncline, Western Guizhou Province, China. Energy Exploration & Exploitation, 30(1): 43-57. (In Chinese with English abstract)

Levine, J.R., 1993. Coalification: The Evolution of Coal as Source Rock and Reservoir Rock for Oil and Gas. In: Law, B.E., Rice, D.D. (Editors), Hydrocarbons from Coal. American Association of Petroleum Geologists, pp. 39-77.

Li, B., 2015. Mineralogy and Geochemistry of Longtan Formation Coals of Late Permian in the Western Guizhou Province, Southwest China. Doctoral Thesis, China University of Geosciences, 115 pp. (In Chinese with English abstract)

Li, J., Bai, P., Mao, H., Han, W., Wang, X., Zhang, J., 2014. Analysis of geochemistry characteristics and its origin of CBM in Zhengzhuang and Hudi blocks. Journal of China Coal Society, 39(9): 1802-1811. (In Chinese with English abstract)

Lippmann-Pipke, J., Sherwood Lollar, B., Niedermann, S., Stroncik, N.A., Naumann, R., van Heerden, E., Onstott, T.C., 2011. Neon identifies two billion year old fluid component in Kaapvaal Craton. Chem. Geol., 283(3): 287-296.

Liu, Q., Wu, X., Wang, X., Jin, Z., Zhu, D., Meng, Q., Huang, S., Liu, J., Fu, Q., 2019. Carbon and hydrogen isotopes of methane, ethane, and propane: A review of genetic identification of natural gas. Earth-Science Reviews, 190: 247-272.

Mark, D.F., Stuart, F.M., de Podesta, M., 2011. New high-precision measurements of the isotopic composition of atmospheric argon. Geochim. Cosmochim. Acta, 75(23): 7494-7501.

McGlade, C., Speirs, J., Sorrell, S., 2013. Unconventional gas – A review of regional and global resource estimates. Energy, 55: 571-584.

McIntosh, J., Martini, A., Petsch, S., Huang, R., Nüsslein, K., 2008. Biogeochemistry of the Forest City Basin coalbed methane play. Int. J. Coal Geol., 76(1): 111-118.

McIntosh, J.C., Warwick, P.D., Martini, A.M., Osborn, S.G., 2010. Coupled hydrology and biogeochemistry of Paleocene–Eocene coal beds, northern Gulf of Mexico. GSA Bulletin, 122(7-8): 1248-1264.

McKavney, R., 2019. Geochemical characteristics of unconventional gas resources in the UK and the applications for gas tracing. Doctoral Dissertation Thesis, University of Edinburgh, 267 pp.

Milkov, A.V., Etiope, G., 2018. Revised genetic diagrams for natural gases based on a global dataset of >20,000 samples. Org. Geochem., 125: 109-120.

Mishima, K., Sumino, H., Yamada, T., Ieki, S., Nagakura, N., Otono, H., Oide, H., 2018. Accurate Determination of the Absolute 3He/4He Ratio of a Synthesized Helium Standard Gas (Helium Standard of Japan, HESJ): Toward Revision of the Atmospheric $^{3}He/^{4}He$ Ratio. Geochemistry, Geophysics, Geosystems, 19(10): 3995-4005.

Moore, M.T., Vinson, D.S., Whyte, C.J., Eymold, W.K., Walsh, T.B., Darrah, T.H., 2018. Differentiating between biogenic and thermogenic sources of natural gas in coalbed methane reservoirs from the Illinois Basin using noble gas and hydrocarbon geochemistry. Geological Society, London, Special Publications, 468.

Moore, T.A., 2012. Coalbed methane: A review. Int. J. Coal Geol., 101: 36-81.

Morrison, P., Pine, J., 1955. Radiogenic origin of the helium isotopes in rock. Ann. N. Y. Acad. Sci., 62(3): 71-92.

Ozima, M., Podosek, F.A., 2002. Noble gas geochemistry. Cambridge University Press, Cambridge

Qin, S., Tang, X., Song, Y., Wang, H., 2006. Distribution and fractionation mechanism of stable carbon isotope of coalbed methane. Science in China Series D: Earth Sciences, 49(12): 1252-1258.

Rice, D.D., 1993. Composition and origins of coalbed gas. In: Law, B.E., Rice, D.D. (Editors), Hydrocarbons from Coal American Association of Petroleum Geologists, pp. 159-184.

Rice, D.D., Clayton, J.L., Pawlewicz, M.J., 1989. Characterization of coal-derived hydrocarbons and source-rock potential of coal beds, San Juan Basin, New Mexico and Colorado, U.S.A. Int. J. Coal Geol., 13(1–4): 597-626.

Scott, J.A. Pujol, M.H.C., Györe, D., Stuart F.M., Gilfillan, S.M.V. (2021). Determining static reservoir connectivity using noble gases. Chemical Geology 582, 120410

Shan, Y., Bi, C., Chi, H., 2018. Geologcial characteristics of coalbed methane and optimization for favorable productive intervals of Yangmeishu syncline in Liupanshui area. Natural Gas Geoscience, 29(1): 122-129. (In Chinese with English abstract)

Shimizu, S., Akiyama, M., Naganuma, T., Fujioka, M., Nako, M., Ishijima, Y., 2007. Molecular characterization of microbial communities in deep coal seam groundwater of northern Japan. Geobiol., 5(4): 423-433.

Smith, S.P., Kennedy, B.M., 1983. The solubility of noble gases in water and in NaCl brine. Geochim. Cosmochim. Acta, 47(3): 503-515.

Strąpoć, D., Mastalerz, M., Dawson, K., Macalady, J., Callaghan, A.V., Wawrik, B., Turich, C., Ashby, M., 2011. Biogeochemistry of Microbial Coal-Bed Methane. Annu. Rev. Earth Planet. Sci., 39(1): 617-656.

Strąpoć, D., Mastalerz, M., Schimmelmann, A., Drobniak, A., Hedges, S., 2008. Variability of geochemical properties in a microbially dominated coalbed gas system from the eastern margin of the Illinois Basin, USA. Int. J. Coal Geol., 76(1): 98-110.

Strąpoć, D., Schimmelmann, A., Mastalerz, M., 2006. Carbon isotopic fractionation of CH_4 and CO_2 during canister desorption of coal. Org. Geochem., 37(2): 152-164.

Tang, S., Tang, D., Xu, H., Tao, S., Li, S., Geng, Y., 2016. Geological mechanisms of the accumulation of coalbed methane induced by hydrothermal fluids in the western Guizhou and eastern Yunnan regions. Journal of Natural Gas Science and Engineering, 33: 644-656.

Tang, X., Wang, Z., Ripepi, N., Kang, B., Yue, G., 2015. Adsorption Affinity of Different Types of Coal: Mean Isosteric Heat of Adsorption. Energy Fuels, 29(6): 3609-3615.

Tishchenko, P., Hensen, C., Wallmann, K., Wong, C.S., 2005. Calculation of the stability and solubility of methane hydrate in seawater. Chem. Geol., 219(1): 37-52.

Torgersen, T., Kennedy, B.M., van Soest, M.C., 2004. Diffusive separation of noble gases and noble gas abundance patterns in sedimentary rocks. Earth Planet. Sci. Lett., 226(3): 477-489.

Vinson, D.S., Blair, N.E., Martini, A.M., Larter, S., Orem, W.H., McIntosh, J.C., 2017. Microbial methane from in situ biodegradation of coal and shale: A review and reevaluation of hydrogen and carbon isotope signatures. Chem. Geol., 453: 128-145.

Wang, L.-J., Yu, J.-H., Griffin, W.L., O'Reilly, S.Y., 2012. Early crustal evolution in the western Yangtze Block: Evidence from U–Pb and Lu–Hf isotopes on detrital zircons from sedimentary rocks. Precambrian Res., 222-223: 368-385.

Wang, Y., Zhu, Y., Liu, Y., Chen, S., 2018. Reservoir characteristics of coal–shale sedimentary sequence in coal-bearing strata and their implications for the accumulation of unconventional gas. Journal of Geophysics and Engineering, 15(2): 411-420.

Wen, H., Jun, L., Huazhou, H., 2008. A Study on Coal Seam Reservoir Characteristics and CBM Exploitation Condition in Baotian-Qingshan Region, Guizhou Coal Geology of China, 20(2): 20-23. (In Chinese with English abstract)

Wetherill, G.W., 1954. Variations in the Isotopic Abundances of Neon and Argon Extracted from Radioactive Minerals. Physical Review, 96(3): 679-683.

Whiticar, M.J., 1996. Stable isotope geochemistry of coals, humic kerogens and related natural gases. Int. J. Coal Geol. 32: 191-215.

Wu, C., Lin, X., Yang, Z., Jin, J., Zhang, Z., 2016. Features and causes of coal measures fluid pressure in Tucheng Syncline Songhe Block of western Guizhou. Coal Science and Technology, 44(10): 88-94. (In Chinese with English abstract)

Wu, C., Yang, Z., Qin, Y., Chen, J., Zhang, Z., Li, Y., 2018. Characteristics of Hydrogen and Oxygen Isotopes in Produced Water and Productivity Response of Coalbed Methane Wells in Western Guizhou. Energy Fuels, 32(11): 11203-11211.

Xia, X., Tang, Y., 2012. Isotope fractionation of methane during natural gas flow with coupled diffusion and adsorption/desorption. Geochim. Cosmochim. Acta, 77: 489-503.

Xu, H., 2012. Geological Theory and Technology for Coalbed Methane Development with Thin and Medium Coal Seam Zones in Guizhou. Doctoral Thesis, China University of Mining and Technology, 171 pp. (In Chinese with English abstract)

Yin, S., Ding, W., Hu, Q., Liu, J., Mei, Y., Liu, Z., 2016. Hydrocarbon source rock characteristics and favorable hydrocarbon-generating area evaluation of Carboniferous-Permian coal measures strata in Qinshui basin, Shanxi, China. Journal of Chengdu University of Technology (Science & Technology Edition), 43(2): 163-176. (In Chinese with English abstract)

Zazzeri, G., Lowry, D., Fisher, R.E., France, J.L., Lanoisellé, M., Kelly, B.F.J., Necki, J.M., Iverach, C.P., Ginty, E., Zimnoch, M., Jasek, A., Nisbet, E.G., 2016. Carbon isotopic signature of coal-derived methane emissions to the atmosphere: from coalification to alteration. Atmos. Chem. Phys., 16(21): 13669-13680.

Zhang, C., 2017. Resource Characteristics and Optimization of Coalbed Methane in Liu Panshui Coalfield. Master Thesis, China University of Mining and Technology, 120 pp. (In Chinese with English abstract)

Zhang, J., Liu, D., Cai, Y., Yao, Y., Ge, X., 2018. Carbon isotopic characteristics of CH_4 and its significance to the gas performance of coal reservoirs in the Zhengzhuang area, Southern Qinshui Basin, North China. Journal of Natural Gas Science and Engineering, 58: 135-151.

Zhang, M., 2019. Coalbed Methane System and Its Developmental Mechanism in Tucheng Syncline, Guizhou, China. Master Thesis, China University of Mining and Technology, 101 pp. (In Chinese with English abstract)

Zheng, J., Griffin, W.L., O'Reilly, S.Y., Zhang, M., Pearson, N., Pan, Y., 2006. Widespread Archean basement beneath the Yangtze craton. Geology, 34(6): 417-420.

Zhou, Z., Ballentine, C.J., 2006. 4He dating of groundwater associated with hydrocarbon reservoirs. Chem. Geol., 226(3–4): 309-327.

Zhou, Z., Ballentine, C.J., Kipfer, R., Schoell, M., Thibodeaux, S., 2005. Noble gas tracing of groundwater/coalbed methane interaction in the San Juan Basin, USA. Geochim. Cosmochim. Acta, 69(23): 5413-5428.

Zhou, Z., Ballentine, C.J., Schoell, M., Stevens, S.H., 2012. Identifying and quantifying natural CO_2 sequestration processes over geological timescales: The Jackson Dome CO_2 Deposit, USA. Geochim. Cosmochim. Acta, 86: 257-275.

Zhuang, X., Querol, X., Zeng, R., Xu, W., Alastuey, A., Lopez-Soler, A., Plana, F., 2000. Mineralogy and geochemistry of coal from the Liupanshui mining district, Guizhou, south China. Int. J. Coal Geol., 45(1): 21-37.

796 **Figures**

797 **Figure 1**

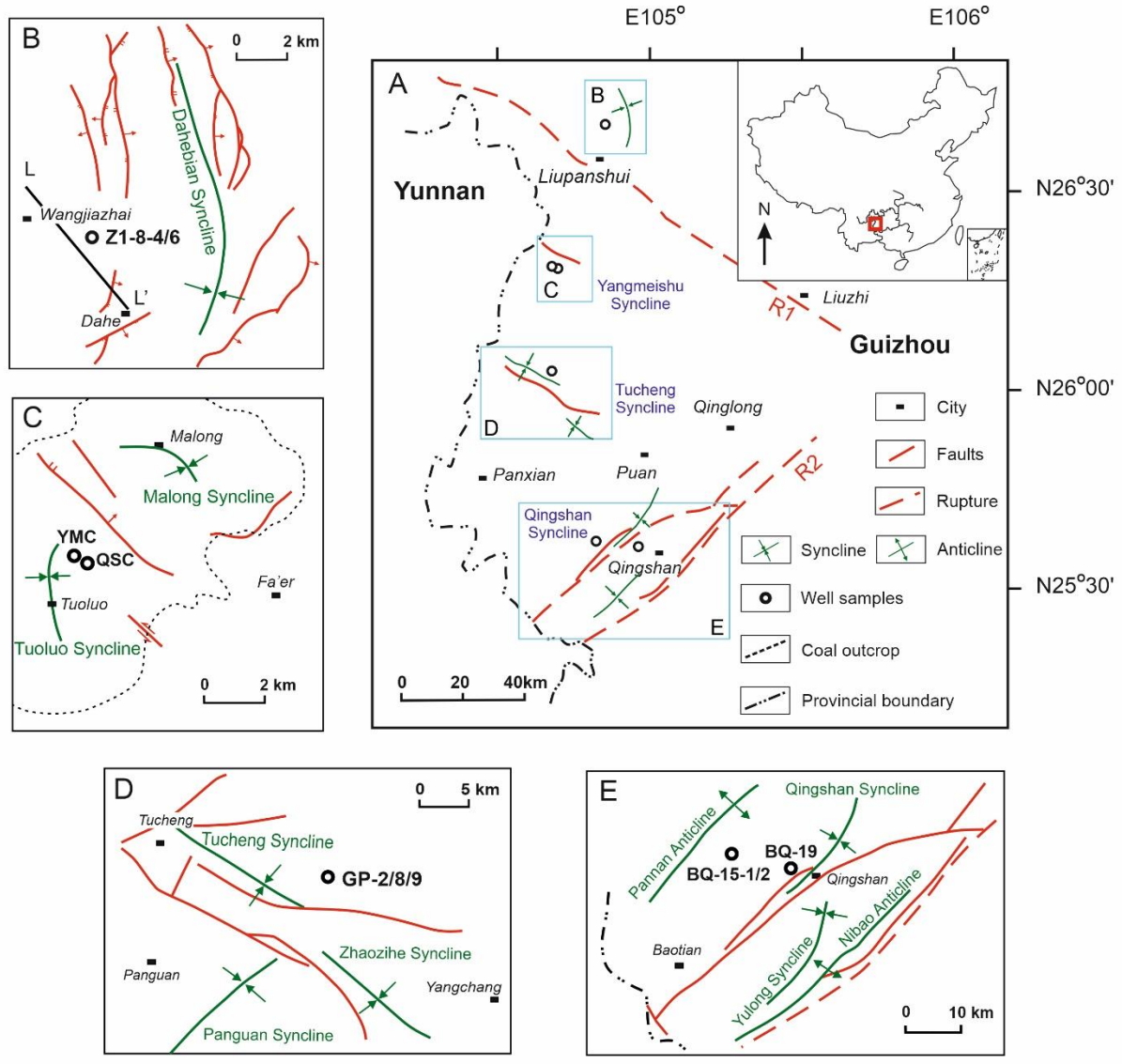

798

799 **Figure 2**

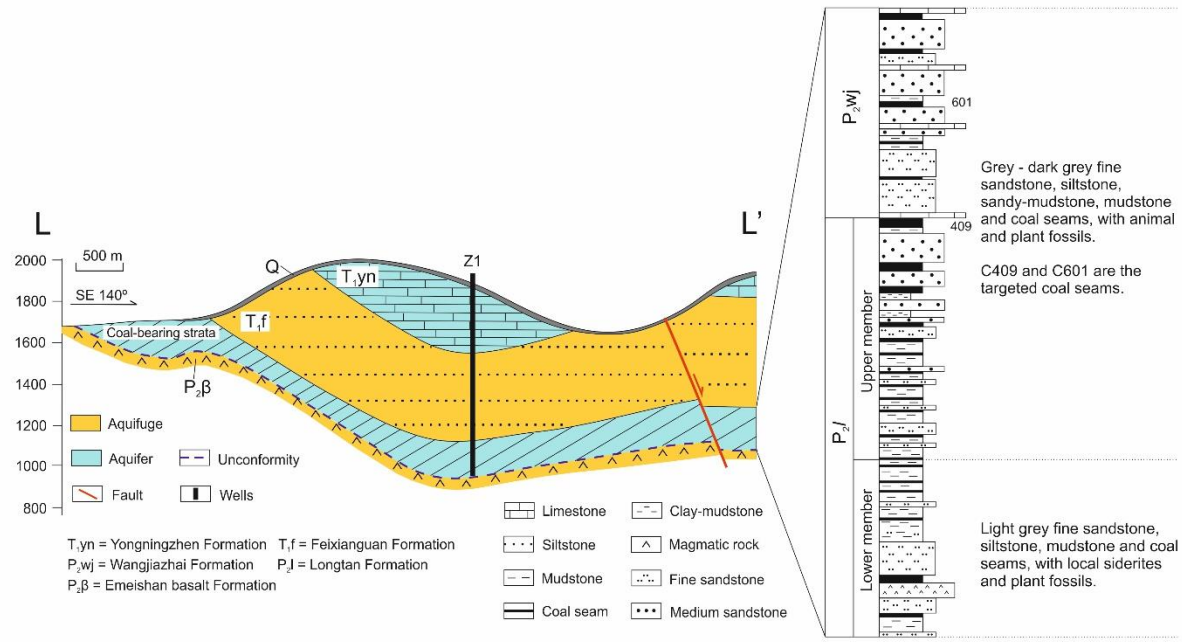

800

Figure 3

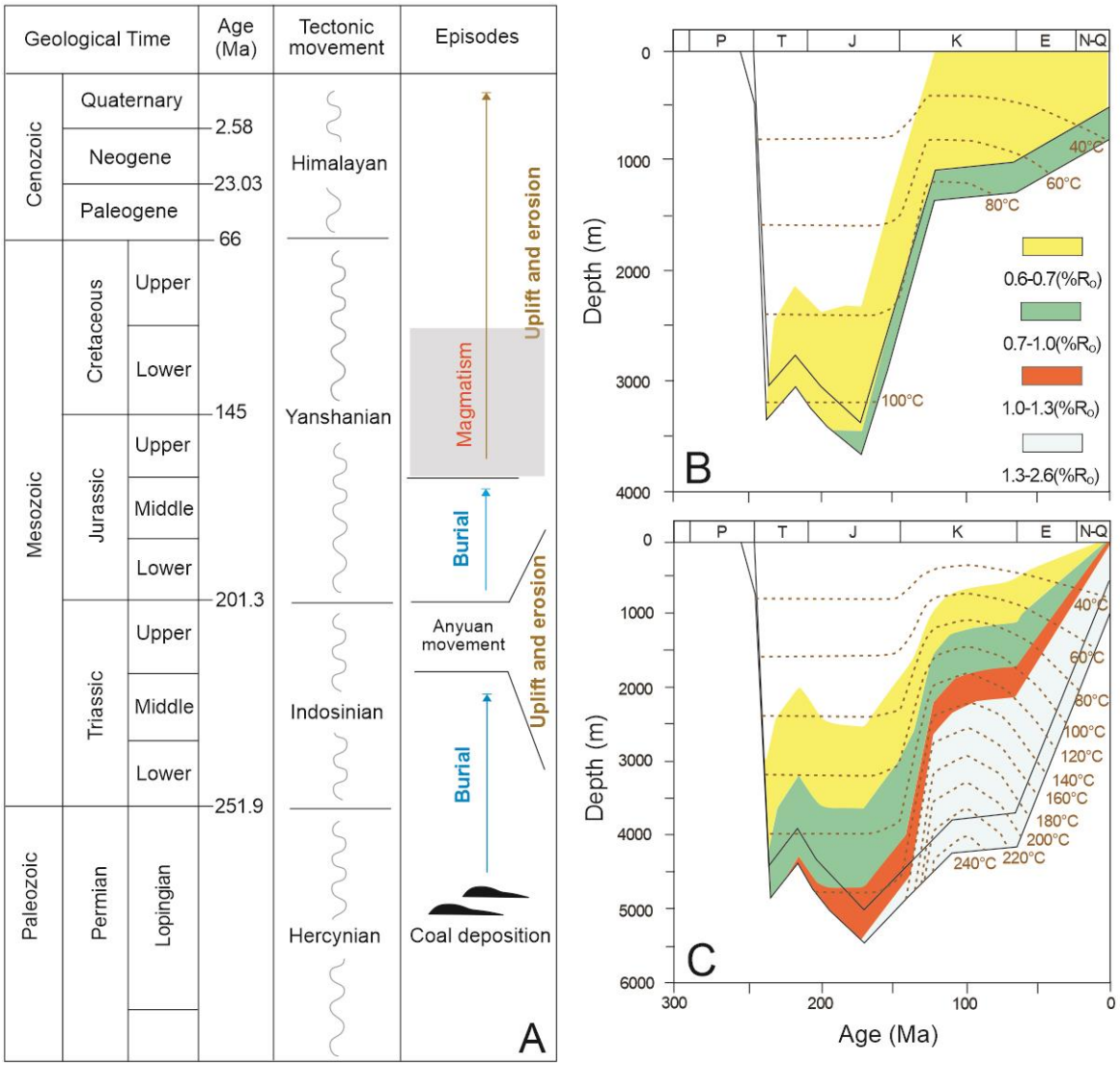
Geological Time
Age (Ma)
Tectonic movement
Episodes
Cenozoic
Quaternary
Neogene
Paleogene
2.58
23.03
66
Mesozoic
Cretaceous
Upper
Lower
145
Jurassic
Upper
Middle
Lower
201.3
Triassic
Upper
Middle
Lower
251.9
Paleozoic
Permian
Lopingian
Himalayan
Yanshanian
Indosinian
Hercynian
Uplift and erosion
Magmatism
Burial
Anyuan movement
Uplift and erosion
Burial
Coal deposition
A
P
T
J
K
E
N-Q
Depth (m)
40°C
60°C
80°C
100°C
0.6-0.7(%Ro)
0.7-1.0(%Ro)
1.0-1.3(%Ro)
1.3-2.6(%Ro)
B
120°C
140°C
160°C
180°C
200°C
220°C
240°C
C
Age (Ma)

803 **Figure 4**

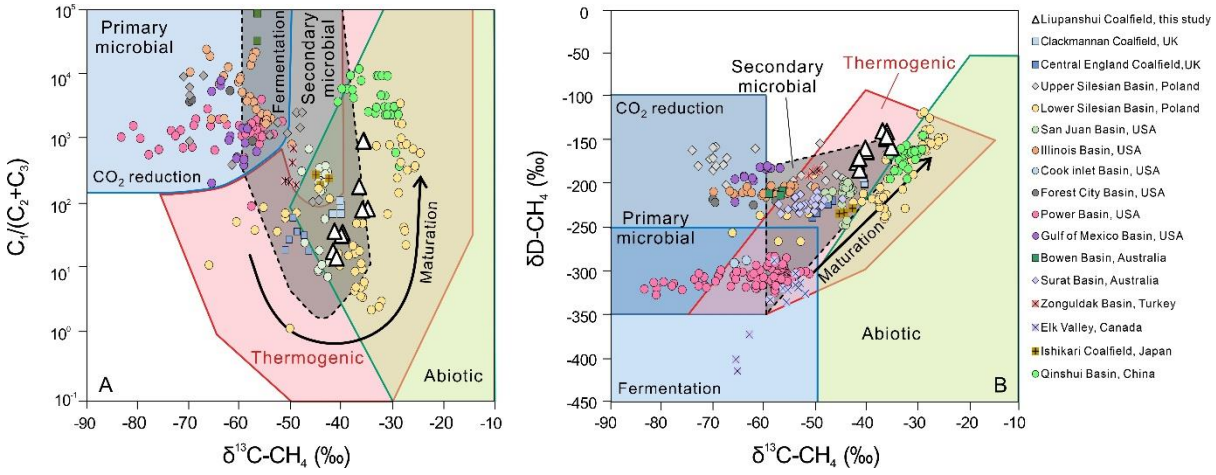

804

805 **Figure 5**

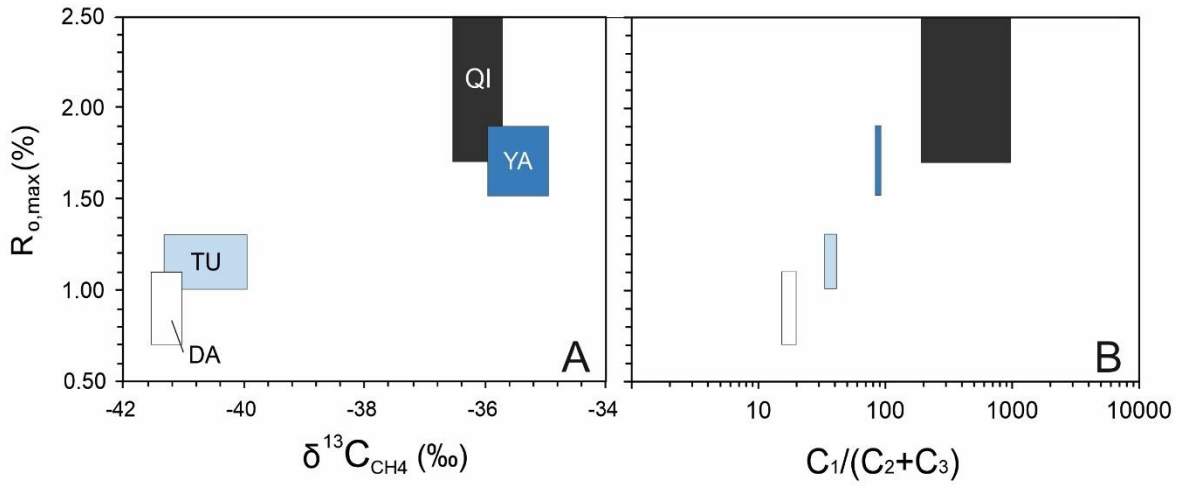

806

807 **Figure 6**

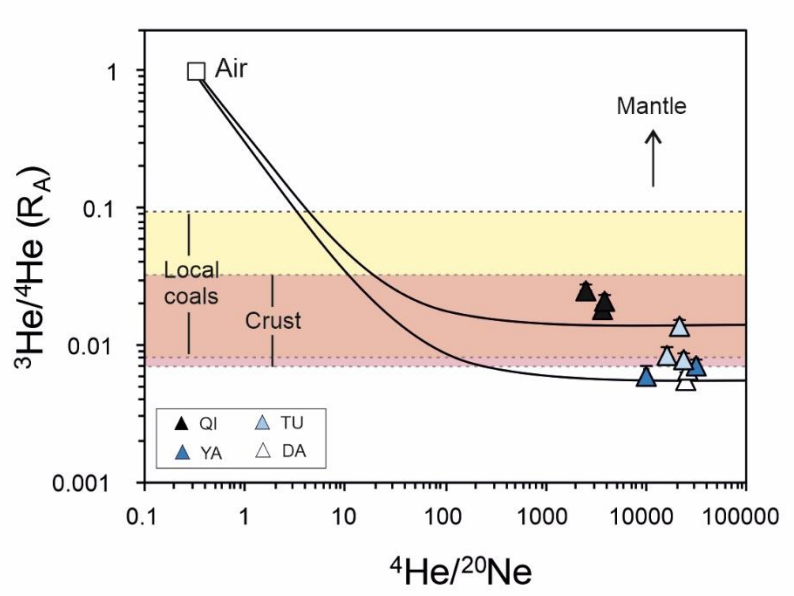

808

809 **Figure 7**

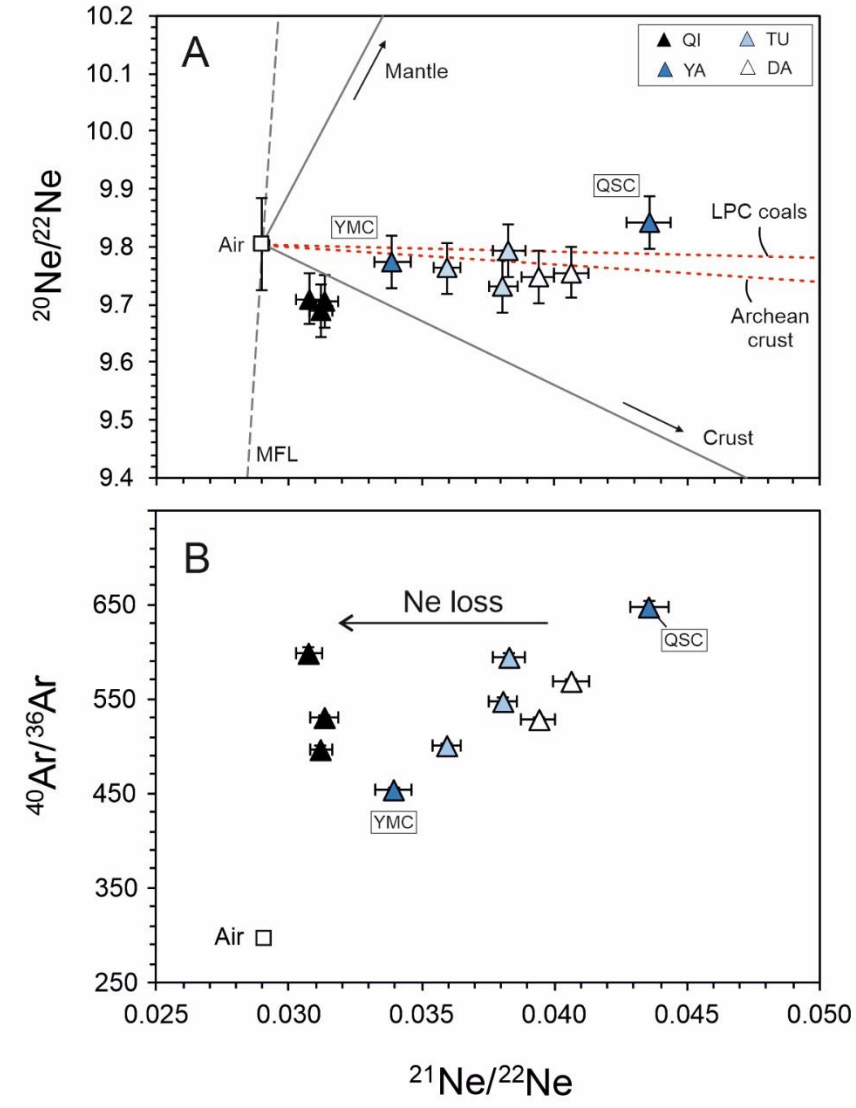

810

811 **Figure 8**

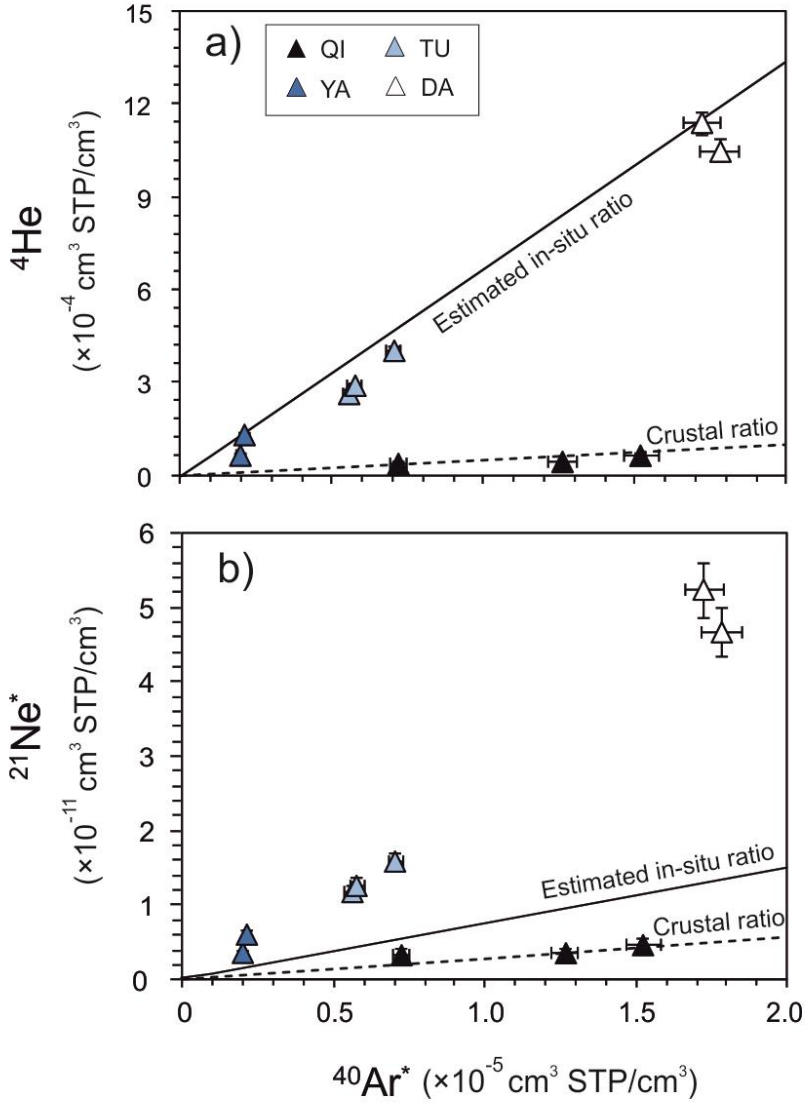

812

813 **Figure 9**

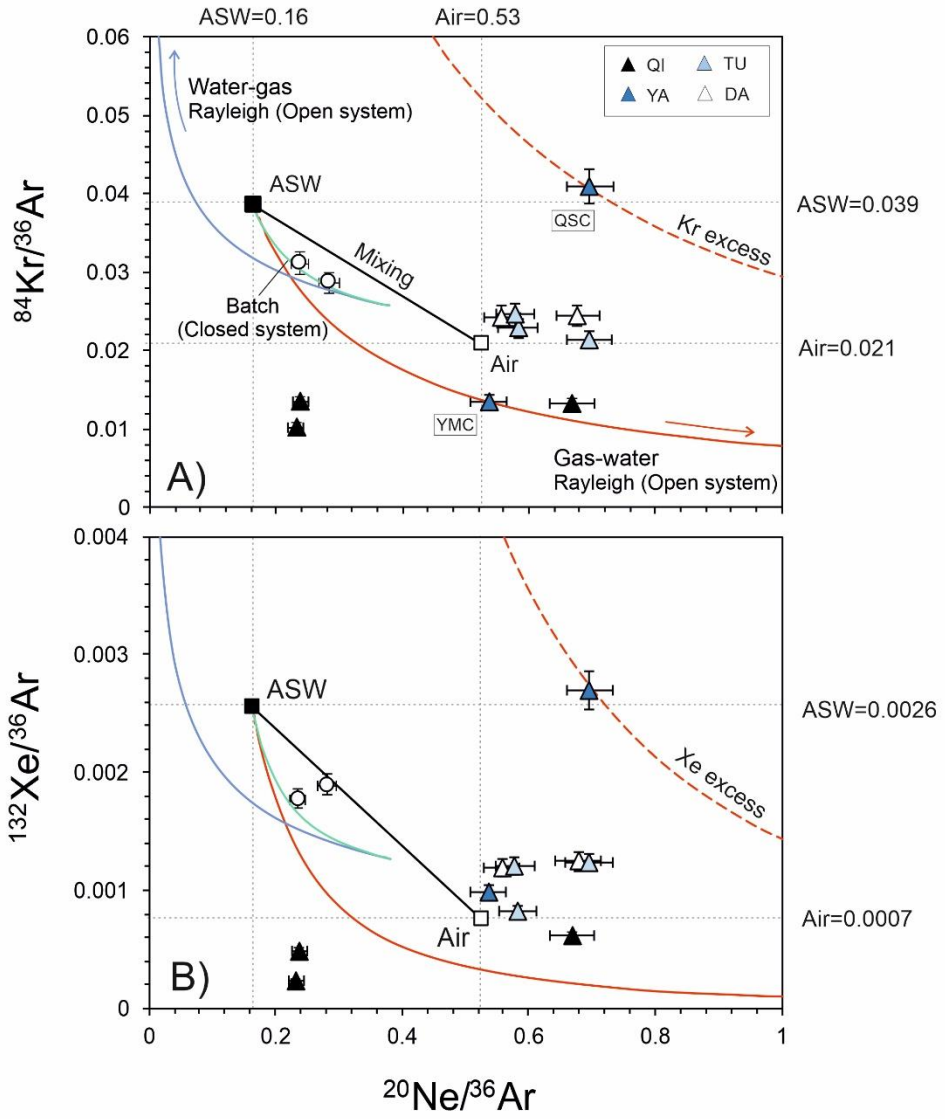

814

Figure 10

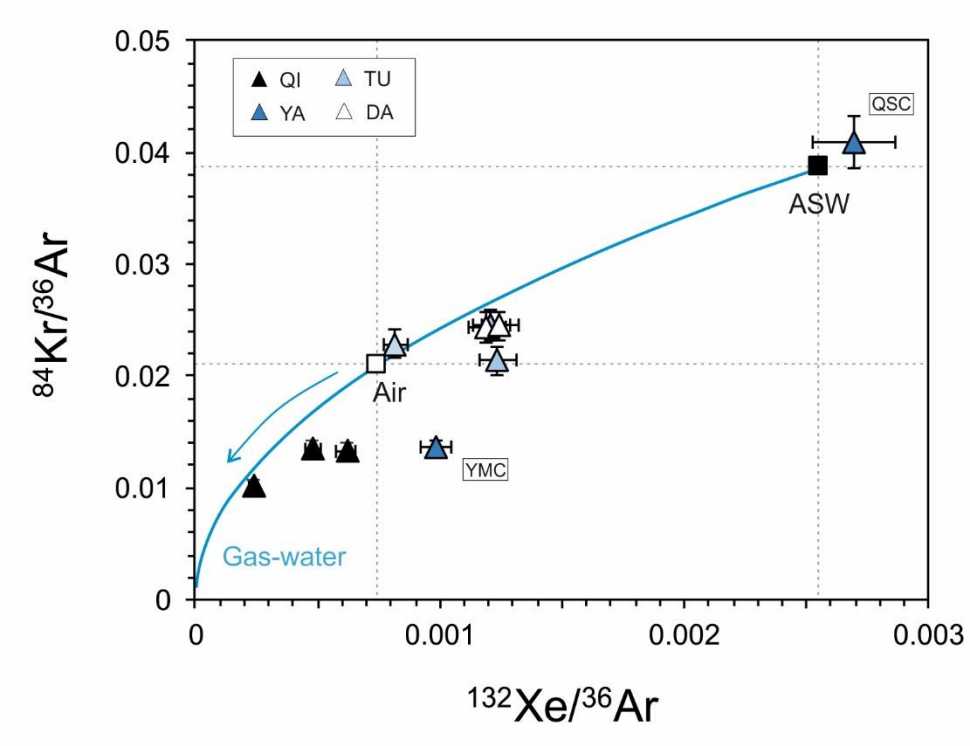
QI
TU
YA
DA
QSC
ASW
Air
YMC
Gas-water
0.05
0.04
0.03
0.02
0.01
0
0
0.001
0.002
0.003
84Kr/36Ar
132Xe/36Ar

Figure Captions

Figure 1. Location of the research area. A. Liupanshui Coalfield showing the blocks sampled in this study; R1, Shuicheng-Ziyun rupture belt; R2, Huangnihe-Panjiazhuang rupture belt after Wu et al. (2018). B-E are expanded views of four blocks from figure A: B. Dahebian block after Bao (2019); C. Yangshumei block after Shan et al. (2018); D. Tucheng block after Wu et al. (2016); E. Qingshan block after Lei et al. (2012).

Figure 2. Transect profile of sediments in Dahebian block of the Liupanshui coalfield and stratigraphic column showing the main coal-bearing strata. Wangjiazhai Formation from the Permian Lopingian in Dahebian block is corresponding to Changxing Formation in the text. Modified from Bao (2019).

Figure 3. A: Stratigraphic column showing the major Mesozoic-Cenozoic burial and erosion episodes of the Liupanshui coalfield. B and C: burial and erosion history of the southern Dahenbian block B), and the eastern Qingshan syncline block C). Redrawn after Dou (2012).

Figure 4. Compilation of molecular and the stable isotopic composition of coal bed methane from LPC. A) $C_1/(C_2+C_3)$ vs. $\delta^{13}C_{CH4}$; B) δD_{CH4} vs. $\delta^{13}C_{CH4}$. LPC data are mainly located in the overlapped zone of thermogenic and secondary microbial methane. Field lines from Milkov and Etiope (2018). Data source: Clackmannan field and Central England filed (Györe et al., 2018), Upper Silesian Basin (Kotarba, 2001), Lower Silesian Basin (Kotarba and Rice, 2001), San Juan Basin(Zhou et al., 2005), Illinois Basin (Moore et al., 2018; Strąpoć et al., 2008), Cook inlet Basin (Dawson et al., 2012), Forest city Basin (McIntosh et al., 2008), Powder Basin (Flores et al., 2008), Gulf of Mexico Basin (McIntosh et al., 2010), Bowen Basin (Kinnon et al., 2010), Surat Basin (Baublys et al., 2015), Zonguldak Basin (Hosgörmez, 2007), Elk Valley field (Aravena et al., 2003), Ishikari Coalfield (Shimizu et al., 2007), Qinshui Basin (Chen et al., 2019; Li et al., 2014; Zhang et al., 2018).

Figure 5. Maximum vitrinite reflectance ($R_{o,max}$) plotted against $\delta^{13}C_{CH4}$ (A) and $C_1/(C_2+C_3)$ (B). The positive relationships between $\delta^{13}C_{CH4}$, $C_1/(C_2+C_3)$ and $R_{o,max}$ of coals in each block indicate that the maturation extent of coals is the main controlling factor on the stable isotopes of methane and major gas composition in the coals.

Figure 6. $^3He/^4He$ ratios plotted against $^4He/^{20}Ne$ ratios for the LPC gases. The solid black lines are mixing lines between air and the highest and lowest values defined by the data. They fall within the range defined by average crust and are predicted to have been generated in the

LPC coals (0.008-0.093 R_A) based on the local range of Li concentration and average large neutron cross-section elements.

Figure 7. Ne-Ar isotopes in LPC gases. (A) $^{20}Ne/^{22}Ne$ vs $^{21}Ne/^{22}Ne$. The excess of nucleogenic Ne is evident in LPC CBM and cannot be explained by the addition of normal crustal Ne. (B) $^{20}Ne/^{22}Ne$ vs. $^{40}Ar/^{36}Ar$. QI block has lower $^{21}Ne/^{22}Ne$ ratios than the other three blocks, while $^{40}Ar/^{36}Ar$ ratios are comparable. MFL (grey dotted line) is the mass fractionation line of Ne. The solid grey lines are air-mantle and air-Phanerozoic crust mixing lines ($^{20}Ne/^{22}Ne_{mantle}$ = 12.5, $^{21}Ne/^{22}Ne_{mantle}$ = 0.06, $^{20}Ne/^{22}Ne_{crust}$ = 0, $^{21}Ne/^{22}Ne_{crust}$ = 0.47; Ballentine et al. (2005); Kennedy et al. (1990)). Mixing lines between air and average local coal ($^{20}Ne/^{22}Ne$ = 1.1, $^{21}Ne/^{22}Ne$ = 11.4), Archaean crust ($^{20}Ne/^{22}Ne$ = 0, $^{21}Ne/^{22}Ne$ = 3.3 ± 0.2; Lippmann-Pipke et al. (2011)) are shown by red dotted lines.

Figure 8. Radiogenic and nucleogenic noble gas isotope abundances in LPC gases. Solid lines indicate the calculated production ratios based on the chemical composition of the local rocks. Dash lines indicate the average crustal ratios. QI gases have evidently lower $^{4}He/^{40}Ar^{*}$ and $^{21}Ne^{*}/^{40}Ar$ ratios compared with TU, DA and YA gases.

Figure 9. The plot of $^{20}Ne/^{36}Ar$ against A) $^{84}Kr/^{36}Ar$ and B) $^{132}Xe/^{36}Ar$ in the LPC well gases. Re-dissolution of exsolved gases from gas to water in an open system can explain the high $^{20}Ne/^{36}Ar$ ratio in LPC gases. However, the samples (except two QI samples) are above the predicted line, indicating that enrichment of ^{84}Kr and ^{132}Xe is required. The lower $^{84}Kr/^{36}Ar$ and $^{132}Xe/^{36}Ar$ than the predicted values in two QI gases indicate the strong adsorption capacity of local coals to the heavy noble gases.

Figure 10. The plot of $^{84}Kr/^{36}Ar$ against $^{132}Xe/^{36}Ar$ in the LPC well gases. Samples are mostly lower than the fractionation line, indicating the excess of ^{132}Xe compared with ^{84}Kr.

871 **Table 1.** Major gas and stable isotope composition of coalbed methane from Liupanshui coalfield, southwest China.

Sample ID	Block	Maximum vitrinite reflectance ($R_{o,max}$/%) [a]	Depth (m)	CH_4 (%)	C_2H_6 (%)	C_3H_8 (%)	CO_2 (%)	Others[b] (%)	$C_1/(C_2+C_3)$	CH_4/CO_2	$\delta^{13}C_{CH4}$ (‰)	δD_{CH4} (‰)
BQ-19	Qingshan block (QI)	1.7-3.0	899	97.1	0.1	-	0.5	2.3	971	194	-35.8	-148
BQ-15-D1			1000	98.3	0.1	-	0.5	1.0	983	192	-35.8	-141
BQ-15-D2			874	96.0	0.5	-	1.2	2.3	192	80	-36.6	-140
1-4-8X	Dahebian block (DA)	0.7-1.1	1200	90.3	3.7	0.9	-	5.1	20	N/A	-41.6	-176
1-6-8X			1150	90.6	4.5	1.1	-	3.8	16	N/A	-41.1	-185
YMC	Yangmeishu block (YA)	1.5-1.9	740	97.7	1.1	-	0.2	1.1	89	489	-34.9	-158
QSC			840	96.5	1.1	-	0.6	1.8	88	161	-35.9	-147
GP-9	Tucheng block (TU)	1.0-1.3	1033	95.0	2.2	0.3	0.1	2.4	38	950	-39.9	-164
GP-8			1062	95.1	2.4	0.3	0.3	1.9	35	317	-40.1	-160
GP-2			953	95.9	2.2	0.2	0.2	1.5	40	480	-41.4	-172

872 1σ standard deviations for major gas abundance, $C_1/(C_2+C_3)$, CH_4/CO_2, $\delta^{13}C$ and δD are 0.3%, 2%, 2%, 0.3‰ and 3‰, respectively.

873 - below detection limit; N/A: not applicable.

874 [a] $R_{o,\,max}$ values are from other studies; QI block (Lei et al., 2012; Wen et al., 2008), DA block (Bao, 2019), YA block (Shan et al., 2018) and TU block (Gui,

875 1999; Dou, 2012).

876 [b] Others include N_2 and O_2.

Table 2. Noble gas compositions of well gases from Liupanshui coalfield, southwest China.

Sample ID	^{4}He ($\times10^{-6}$)	^{20}Ne ($\times10^{-8}$)	^{40}Ar ($\times10^{-5}$)	^{84}Kr ($\times10^{-10}$)	^{132}Xe ($\times10^{-11}$)	$^{3}He/^{4}He$ (R/R_A)	$^{20}Ne/^{22}Ne$	$^{21}Ne/^{22}Ne$	$^{40}Ar/^{36}Ar$	$^{38}Ar/^{36}Ar$
BQ-19	47 (2)	1.30 (5)	2.89 (10)	7.3 (3)	2.6 (1)	0.017 (1)	9.71 (5)	0.0313 (5)	530 (3)	0.187 (1)
BQ-15-D1	41 (1)	1.61 (6)	1.44 (5)	3.2 (1)	1.5 (1)	0.025 (1)	9.71 (5)	0.0308 (5)	598 (7)	0.187 (1)
BQ-15-D2	68 (2)	1.78 (7)	3.82 (14)	7.8 (3)	1.8 (1)	0.021 (2)	9.69 (5)	0.0312 (4)	497 (3)	0.185 (1)
1-4-8X-1	1048 (34)	4.32 (16)	4.09 (15)	18.8 (8)	9.2 (5)	0.005 (1)	9.75 (5)	0.0394 (6)	529 (2)	0.189 (1)
1-6-8X-1	1136 (37)	4.34 (16)	3.63 (13)	15.6 (6)	8.0 (4)	0.006 (1)	9.76 (5)	0.0406 (7)	568 (4)	0.188 (1)
YMC	67 (2)	0.68 (3)	0.58 (2)	1.7 (1)	1.3 (1)	0.006 (1)	9.77 (5)	0.0339 (7)	454 (3)	0.188 (1)
QSC	133 (4)	0.42 (2)	0.39 (1)	2.5 (1)	1.6 (1)	0.007 (1)	9.84 (5)	0.0436 (8)	647 (6)	0.187 (1)
GP-9	401 (13)	1.66 (6)	1.42 (5)	5.1 (2)	3.0 (1)	0.008 (1)	9.79 (5)	0.0383 (6)	593 (5)	0.187 (1)
GP-8	266 (9)	1.62 (6)	1.39 (5)	6.3 (3)	2.3 (1)	0.008 (1)	9.76 (5)	0.0359 (5)	500 (4)	0.187 (1)
GP-2	289 (9)	1.34 (5)	1.27 (5)	5.7 (2)	2.8 (1)	0.013 (1)	9.73 (5)	0.0381 (5)	548 (4)	0.187 (1)
Air	5.24 (5)	1645 (4)	934 (1)	6498 (57)	2339 (27)	1.000 (9)	9.80 (8)	0.0290 (3)	298.6 (3)	0.1885 (3)

1σ standard deviation is shown as the last significant figures in parentheses.

Noble gas concentrations are in unit of cm^3 STP/cm^3 with standard conditions after (Ozima and Podosek, 2002) (p =0.101 MPa, T = 0 °C).

Air composition is after Eberhardt et al. (1965); Györe et al. (2019); Mark et al. (2011); Ozima and Podosek (2002).

R_A is the atmospheric $^{3}He/^{4}He$ ratio of 1.34×10^{-6} (Mishima et al., 2018).

882 **Table 3.** Radiogenic and nucleogenic noble gas composition.

Sample ID	$^{21}Ne^{*}$ ($\times10^{-12}$)	$^{40}Ar^{*}$ ($\times10^{-6}$)	$^{4}He/^{40}Ar^{*}$	$^{21}Ne^{*}/^{40}Ar^{*}$ ($\times10^{-6}$)	$^{4}He/^{21}Ne^{*}$ ($\times10^{7}$)
BQ-19	3.5 (7)	12.6 (5)	3.7 (2)	0.27 (6)	1.4 (3)
BQ-15-D1	3.3 (9)	7.2 (3)	5.7 (3)	0.46 (12)	1.2 (3)
BQ-15-D2	4.6 (9)	15.2 (6)	4.5 (2)	0.30 (6)	1.5 (3)
1-4-8X	47 (3)	17.8 (7)	58 (3)	2.6 (2)	2.2 (2)
1-6-8X	52 (4)	17.3 (6)	66 (3)	3.0 (2)	2.2 (2)
YMC	3.5 (5)	2.0 (1)	34 (2)	1.8 (3)	1.9 (3)
QSC	6.1 (4)	2.1 (1)	63 (3)	2.9 (2)	2.2 (2)
GP-9	16 (1)	7.1 (3)	57 (3)	2.2 (2)	2.5 (2)
GP-8	12 (1)	5.6 (2)	48 (2)	2.1 (2)	2.3 (2)
GP-2	13 (1)	5.8 (2)	50 (2)	2.2 (2)	2.3 (2)

883 1σ standard deviation is shown as the last significant figures in parenthese

884 **Table 4.** Parameters and results for methane loss estimation.

Block	Porosity	Heat of adsorption (kJ/mol)	Burial depth (m)		P (MPa)	T (°C)	n_{free} ⁑ (mol/m^3)	n_{ad} ‡ (mol/m^3)	Fraction of free gas loss	Fraction of total gas loss
QI	0.04[a]	22.2[c]	before	5000	49	167	522	1030	0.77	0.25
			after	800	8	41	121	1051		
DA	0.07[b]	15.1[d]	before	3500	34	122	717	843	0.64	0.31
			after	1000	10	47	259	811		

885 [a] Huang and Qu (2021).

886 [b] Bao (2019).

887 [c] Tang et al. (2015).

888 [d] Xia and Tang (2012).

889 ⁑ the concentration of free gas in rock.

890 ‡ the concentration of adsorbed gas in rock.

891 **Table 5.** Calculated volumetric groundwater/gas ratios in two-stage fractionation processes.

Sample ID	$^{20}Ne/^{36}Ar$	Fraction of ^{36}Ar re-dissolved in groundwater	Initial ^{36}Ar in gas phase cm^3 STP/cm^3 ($\times 10^{-7}$)	Stage1 V_w/V_g (STP)	Stage2 V_w/V_g (STP)
BQ-19	0.24	0.49	1.06	0.11	0.31
BQ-15-D1	0.67	0.92	2.90	0.29	1.15
BQ-15-D2	0.23	0.46	1.42	0.14	0.29
1-4-8X	0.56	0.89	6.75	0.68	1.00
1-6-8X	0.68	0.92	7.88	0.79	1.16
YMC	0.54	0.88	1.03	0.10	0.97
QSC	0.69	0.92	0.77	0.08	1.18
GP-9	0.70	0.92	3.08	0.31	1.18
GP-8	0.58	0.89	2.62	0.26	1.04
GP-2	0.58	0.89	2.15	0.22	1.03

892